UCRL-CR-130728
B334423

BBN Technical Memorandum W1303

Hydroacoustic Propagation Grids for the CTBT Knowledge Database

J. Angell
T. Farrell
K. LePage

May 1998

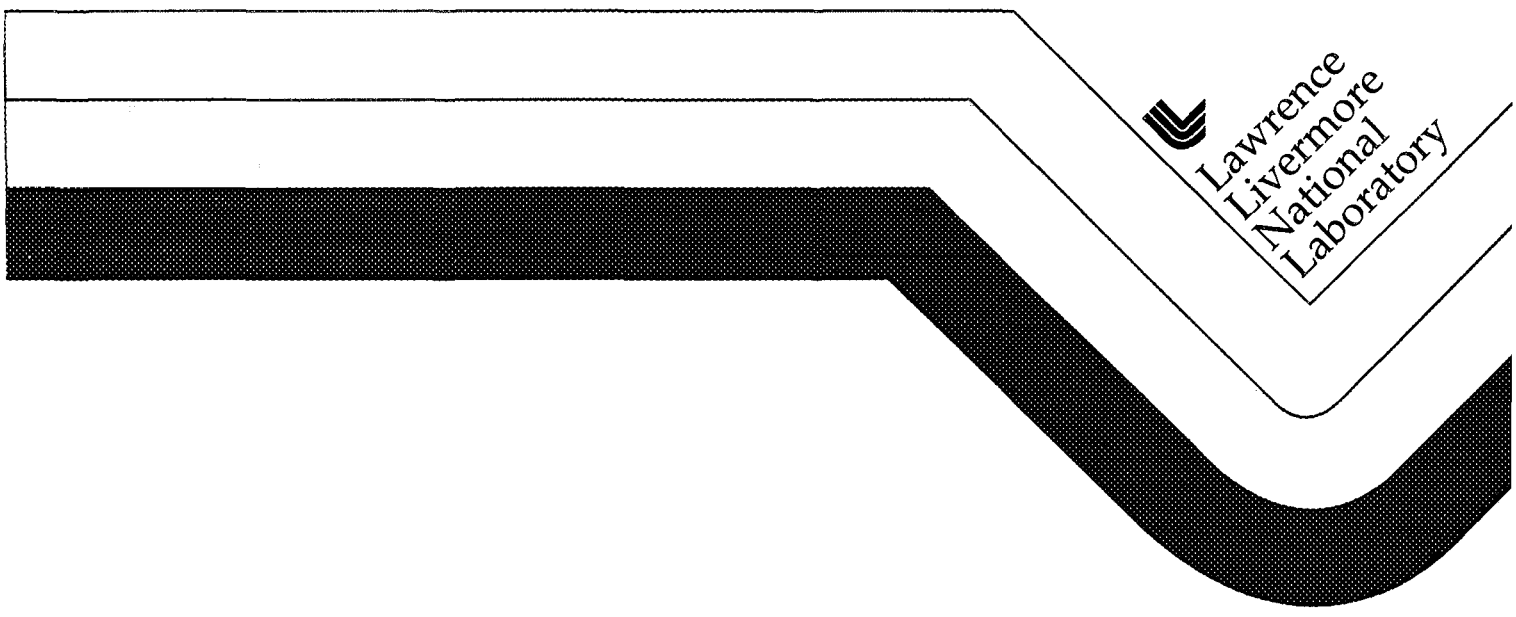

Work performed under the auspices of the U.S. Department of Energy by Lawrence Livermore National Laboratory under Contract W-7405-ENG-48.

BBN Technical Memorandum W1303

Hydroacoustic Propagation Grids for the CTBT Knowledge Database

October 1997

Jeff Angell
Ted Farrell
Kevin LePage

Sub Contract B334423

Prepared By: BBN Systems and Technologies
1300 North 17th Street
Arlington, VA 22209

Prepared For: Lawrence Livermore National Laboratory
PO Box 808, L-205
Livermore, CA 94551

Abstract

The Hydroacoustic Coverage Assessment Model (HydroCAM) has been used to develop components of the hydroacoustic knowledge database required by operational monitoring systems, particularly the US National Data Center (NDC). The database, which consists of travel time, amplitude correction and travel time standard deviation grids, is planned to support source location, discrimination and estimation functions of the monitoring network. The grids will also be used under the current BBN subcontract to support an analysis of the performance of the International Monitoring System (IMS) and national sensor systems. This report describes the format and contents of the hydroacoustic knowledgebase grids, and the procedures and model parameters used to generate these grids. Comparisons between the knowledge grids, measured data and other modeled results are presented to illustrate the strengths and weaknesses of the current approach. A recommended approach for augmenting the knowledge database with a database of expected spectral/waveform characteristics is provided in the final section of the report.

Keywords: hydroacoustics, network, localization, oceanography, performance prediction

Table of Contents

1.0 Introduction

This report summarizes work performed under contract to Lawrence Livermore National Laboratory during the period 1 January to 30 September 1997. The main goal of the effort is to use the Hydroacoustic Coverage Assessment Model (HydroCAM) to develop components of the hydroacoustic knowledge database required by operational monitoring systems, particularly the US National Data Center (NDC). The grids, which consist of travel time, amplitude correction and travel time standard deviation grids, are planned to support source location, discrimination and estimation functions. These grids will also be used under the current BBN subcontract to support an analysis of the performance of the International Monitoring System (IMS) and national sensor systems.

The purpose of this report is to:

(1) Describe the format and contents of the hydroacoustic knowledgebase grids generated under this effort. These grids include travel time, range, amplitude correction and travel time standard deviation. The procedure and parameters used to generate these grids is also provided.

(2) Summarize comparisons between the knowledge grids, measured data and other modeled results to illustrate the strengths and weaknesses of the current approach.

(3) Summarize the feasibility and recommended approach for augmenting the knowledge database with a database of expected spectral/waveform characteristics.

2.0 The hydroacoustic grids

During the HydroCAM development effort in 1995-96, a number of global-scale low-frequency propagation modeling approaches were investigated [1]. The primary conclusions were:

(1) The simplest reasonable propagation model must account for the ellipsoidal nature of the earth and the geographic and seasonal variations in the SOFAR channel sound speed. This model can accurately predict paths and travel times for large expanses of the ocean, primarily open ocean, mid-latitude waters.

(2) The effects of horizontal refraction are required for cases where paths interact with bathymetric features such as continental shelves, islands and seamounts, and when paths traverse rapidly changing water, such as the Antarctic convergence. Furthermore, reported data in the literature suggests that modal phase speeds (vs channel sound speeds) are required to accurately predict the horizontal refraction [2].

(3) The most efficient model for including horizontal refraction will likely use the WKB approximation for the calculation of the acoustic phase velocities, and a boundary value approach to finding refracted rays connecting two points.

(4) Travel time variance can be modeled reasonably well using the available historical databases of sound channel fluctuations.

While the general form of the model to be used for generating the knowledgebase was determined, the specific spatial resolutions, geographic databases and other computational parameters necessary to generate the grids for the knowledge database were not specified. Much of this report summarizes the studies performed to select these parameters.

As seen above, the model generally breaks up the three-dimensional nature of the propagation into a vertical component (SOFAR channel sound speeds or normal modes) followed by a horizontal component (geodesic or refracted paths on an ellipsoidal earth). Results in [2] indicate that a model which includes horizontal refraction and uses normal modes to accurately calculate the vertical component of the ocean waveguide (as opposed to assuming that all the energy propagates in the SOFAR channel) is needed to predict travel times for nearly antipodal paths which traverse Antarctic regions. In this approach, each individual geographic location in the ocean is treated as a range independent waveguide. In our work, it is further assumed that mode 1 provides the dominant portion of the acoustic path propagation needed for travel time estimation, since in most cases it will have the least amount of interaction with the ocean surface and bottom among all the modes. Thus, in generating the knowledgebase grids, all calculations will use only the first normal mode to characterize the ocean waveguide.

The knowledgebase grids will be generated for winter, spring, fall and summer to account for seasonal fluctuations in the sound velocity profiles and for two frequencies: 10 Hz and 50 Hz. The motivation for these particular frequencies is that most of the energy contained in the acoustic signature for earthquakes is less than 20 Hz; whereas for most explosions the dominant energy is above 20 Hz.

2.1 Grid Definitions and Format

There are several sets of grids which are to be generated. In this effort, the term *grid* refers to both a specific data structure and data file format. Functionally, a grid is defined as a matrix of floating point numbers which contain data over a rectangular region in latitude/longitude space, with latitude in rows and longitude in columns. The data starts at the southwest corner of the region, and works to the east and then north. (See Figure 1). All lat/lon values are referenced to the center of the cells.

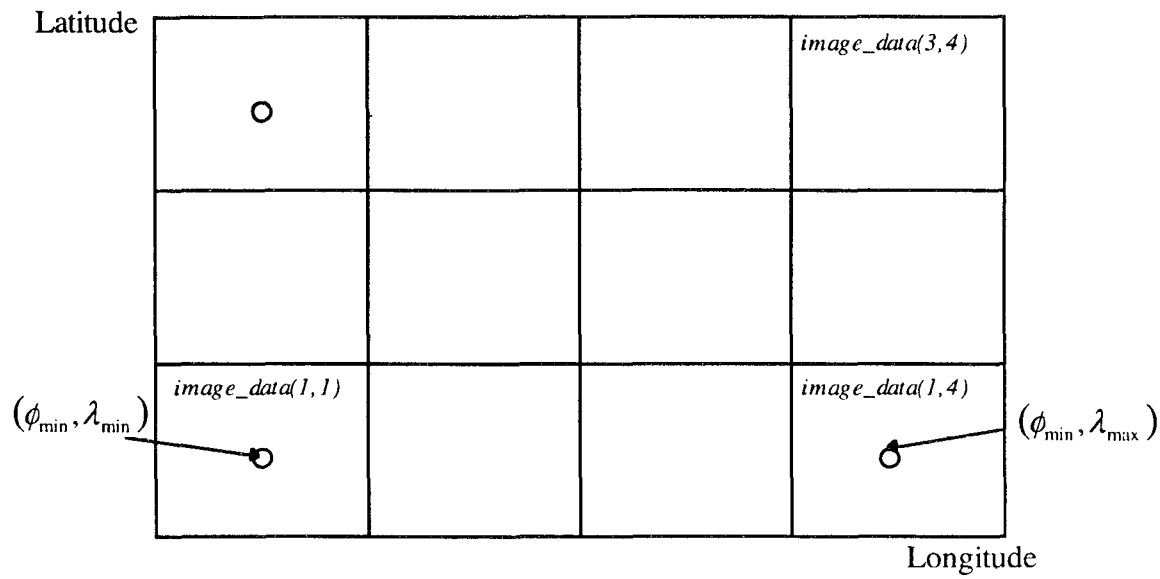

Figure 1: HydroCAM Grid Data Structure

The set of grids which are to be delivered as part of the hydroacoustic knowledgebase are the four ***Propagation Grids***, or knowledgebase grids. These grids contain the travel time, range, attenuation, and travel time standard deviation as predicted from a given station to all source locations on the grid. The equations used to determine the these quantities are contained in the *HydroCAM Users Guide [3]*. Some additional propagation grids are also being delivered. The purpose of the additional grids is to enhance the interpretation of the grids listed above, and to allow network performance predictions to be performed. A

listing of the propagation grids delivered under this effort is provided in Table 1. The second set of grids are called ***Modal Property Grids***, or simply modal grids. These grids are required by the raytrace program used to generate the propagation grids. The four modal grids include phase speed, group speed, modal attenuation and modal slowness variance.

Table 1: Propagation Characteristic Grids

Grid Name	File Extension	Purpose
Travel Time	.TTgrid	Localization algorithms
Travel Time Std. Dev.	.STgrid	Network AOU calculations
Range	.Rgrid	Compute baseline path attenuation
Attenuation Correction	.ATTENgrid	Compute total attenuation
Multipath	.MPgrid	Indicate presence of multiple paths
Launch Angle	.ANGLEgrid	SNR calculation
Transmission Loss	.TLgrid	SNR calculation

The data in each of these grids is stored in a set of grid files. Grid files are an integral part of the *GridDB* object class used in HydroCAM, and much of the interface software is contained in *GridDB.cc*. Grid files consist of a header followed by a number of data blocks that contain the data on the grid. The data block consists of *Nlats*Nlons* single-precision floating point numbers. They are written from the south-west corner of the grid. All points in the first row (latitude) are followed by all points in the next latitude. If multiple grids are contained in the file, they are provided in sequence. The format of the 48 byte header is provided in Table 2.

Table 2: Format of Grid File Header

Header Variable	*Description*	*Type*
Nlats	number of latitudes (rows) in the grid	4-byte integer
Nlons	number of longitudes (columns) in the grid	4-byte integer
latBase	latitude of the center of the southernmost grid cell	double
lonBase	longitude of the center of the westernmost grid cell	double
latInc	latitude resolution (degrees)	double
lonInc	longitude resolution (degrees)	double
ngrids	number of grids in the grid file	4-byte integer
wrap_flag	indicates whether the 1st column should be considered next to the last column (wraparound in longitude)	4-byte integer

The grids can be accessed in the following ways:

1) Using the "Prop/Det" form in HydroCAM, load the desired grid using the "Load" button, then display it using the "Display" button.

2) From the MATLAB command line, use the function *read_GridDB.m* provided with HydroCAM to load the data into the MATLAB workspace.

3) Use the GridDB object class in a short C++ program to load the data.

2.2 Summary of procedure and parameters

The grid generation procedure consists of three steps, as shown in Figure 2. The first step is to generate the modal grids, ie phase speed, group speed, modal attenuation (due to bottom interaction) and group slowness variance. These grids are generated for each season at 1 degree resolution for world-wide coverage and higher resolution for local areas where it is expected that phase speeds will change significantly. The primary inputs for generating these grids are the environmental databases for bathymetry, sound speed and sound speed standard deviation. Several databases for each type (which have various degrees of geographic coverage, temporal coverage and resolution) have been incorporated into HydroCAM.

The second step is to use the modal property grids to compute the travel time, path attenuation and travel time standard deviation along horizontally refracted paths from each station in the monitoring network. Energy loss due to ice cover and the ocean bottom are integrated along each path. Loss terms with analytic range dependence (such as cylindrical spreading) are separated from this integration, and the distance along the path saved in order to allow standard path attenuation models to be used post-priori. These non-uniformly sampled "path files" are then interpolated in the final step onto a regular latitude/longitude grid to produce the propagation characteristic grids for the knowledge database. Sections 2.3 and 2.4 provides details on the procedures which will be used to generate the modal property and the propagation characteristics grids respectively.

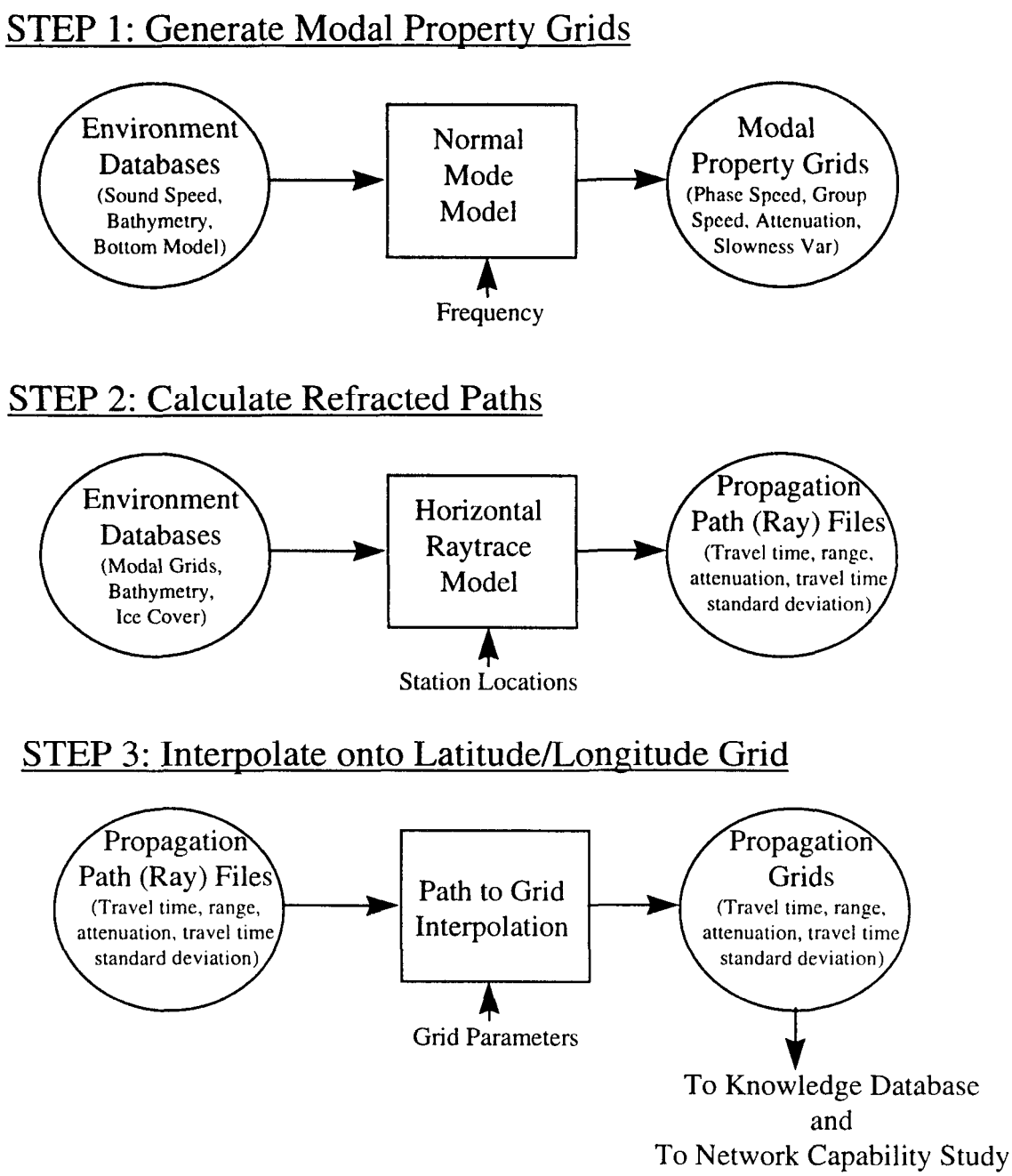

Figure 2: Summary of Grid Generation Procedure

2.3 Modal Property Grids

Before generating the modal property grids, several issues need to be addressed. These include determination of geographic regions which may require higher resolution than that provided by the nominal 1° resolution used for the world-wide grids, selection of an appropriate acoustic mode model (Kraken or WKB), the selection of environmental databases (bathymetry, sound speed, sound speed standard deviation), and determination of specific grid parameters. Table 3 summarizes the databases and parameters that will be used to generate the modal grids for both the world-wide and high-resolution areas. The following paragraphs detail the rationale behind selecting these databases and parameters.

2.3.1 Determination of High-Resolution Areas

One of the first steps in generating the modal property grids is to identify geographic regions which may require finer resolution than provided by nominal 1° world-wide grid resolution. These areas include regions near islands or coastlines where ray paths originating from monitoring stations are likely to interact with bathymetric features. In these regions the paths themselves, as well as travel time and attenuation estimates along the paths, will be significantly affected due to rapid changes in bathymetry and sound velocity structure.

The first step was to analyze preliminary raytraces produced in 1995 by the Naval Research Laboratory (NRL) for the Department of Energy for each of the candidate IMS stations. The purpose of this analysis was to locate the general regions where land/island refraction and blockage were likely to have a significant effect on the ray paths. Each of the identified regions fell into one of five categories:

1. Coastal regions with near-grazing ray paths, especially regions where the bottom depth was less than 1500 meters,
2. Large islands (eg. Kerguelen or Hawaii) which could cause total ray blockage as well as ray bending,
3. Central ocean areas which were located near IMS stations (eg. Crozet Island),
4. Clusters of small islands (eg. Marshall Islands), and
5. Isolated small islands (eg. Samoa).

Table 3: Parameters for Modal Property Grids

	WORLD-WIDE (1 degree resolution)			HIGH-RESOLUTION (5 minute resolution)		
Region	Latitude (N) -80.5 to 89.5	Longitude (E) -179.5 to 179.5		See Table 4		
Environment						
	Database[1]	Interp[2]	Season[3]	Database[4]	Interp	Season
Bathy:	E	T	N/A	E and S	T and B	N/A
SSP:	W1	T	All	W1 and G	L	All
STD:	W5	T	Annual	W5	T	Annual
Bottom[5]:	Fluid Half Space	N/A	N/A	Fluid Half Space	N/A	N/A
Mode Model Parameters						
Model	WKB			WKB/Kraken[4]		
Water Density	1.027 (gm/cm3)			1.027 (gm/cm3)		
Mode Number	1			1		
Cutoff Depth	111 m			111 m		
Frequencies	10 and 50 Hz			10 and 50 Hz		
Mode Depth Increment (m)	10 (for 10 Hz), 2 (for 50 Hz)			10 (for 10 Hz), 2 (for 50 Hz)		

Notes:

1) Database Abbreviations E = ETOPO5, S=Scripps, W1 = World Ocean Atlas (WOA) 1 degree resolution, W5 = WOA 5 degree resolution, G = Generalized Digital Environmental Model (GDEM)

2) Interpolation Methods: T = Table Look-Up (used for E, W1 and W5 databases), B = Bi-Linear (used for S), L = Linear (used for both W1 and G for High-Resolution areas only)

3) Seasons are Winter (Jan-Mar), Spring (Apr-Jun), Summer (Jul-Sep), Fall (Oct-Dec)

4) See Table 4 for specific databases and modal model used for each high-resolution area

5) Bottom Model Parameters for all areas (see text)

sound speed	1550 m/sec
density	1.5405 gm/cm3
attenuation	0 015 dB/λ

Regions where the fluctuations in bathymetry or sound speed (and therefore variations in phase speed) were adequately characterized by the 1 degree database (eg. the Aleutian Islands and Tonga Ridge) were removed from consideration. Finally, the local bathymetry of each region was investigated to determine the specific boundaries necessary. The results of this analysis were fifty one regions identified as high-resolution areas, as listed in Table 4. Figure 3 shows the geographic location of each region.

During the raytracing/interpolation portions of the grid generation procedure, other regions may be identified that require high-resolution modal grids. Also, if stations are added or relocated in the future, then additional high-resolution areas may need to be considered as well.

2.3.2 Acoustic Mode Model

Kraken is a well known finite difference model [4] which computes the normal mode structure (eigenfunctions (mode shapes) and eigenvalues). Kraken has been integrated into HydroCAM such that it can be run at each point on a geographic grid. However, since Kraken computes all the mode shapes and eigenvalues which lie between specified phase velocity limits, it is computationally intensive. An alternative to Kraken is a WKB finite difference model which estimates the eigenvalues using a standard WKB approximation and then computes the mode shapes and refines the eigenvalue estimate [3]. The WKB approximation is valid if the variation in the vertical wavenumber is small over a vertical wavelength. This model was developed and integrated under the 1996 HydroCAM effort.

The primary advantage of using WKB over Kraken is that it computes the eigenfunctions and eigenvalues only for modes that are specifically requested by the user, which results in a significant time savings. For example, the execution time for Kraken on a SPARC20 workstation to generate modal parameters for a sample world-wide grid (1 degree resolution, Mode 1, 10 Hz) was 13 hours, whereas WKB took only 20 minutes for the same scenario. A potential disadvantage of using WKB is that its approximation may cause inaccuracies in the modal grids. A number of general comparisons of world-wide phase speeds and refracted ray locations were performed last year [1] which indicated great promise of the WKB approach. Here we perform additional comparisons between the modal grids generated by Kraken and WKB for several cases; to verify that the attenuation and group speed parameters are also accurately calculated, and to verify that WKB works well for shallow water/high-resolution grids.

Table 4 (Part 1): High Resolution Areas

Grid Name and Number	Latitude (N)		Longitude (E)		Data*		Model+
1. Cape Horn	-54.50	-57.50	-74.50	-62.50	S	G	K
2. Palmerland	-60.50	-70.50	-75.50	-49.50	E	W	K
3. Cape of Good Hope	-31.50	-37.50	14.50	25.50	E	G	W
4. Enderby Land	-64.50	-67.50	44.50	60.50	E	W	W
5. Queen Mary Coast	-62.50	-67.50	94.50	105.50	E	W	W
6. Kerguelen Islands	-46.00	-54.50	65.50	78.50	E	W	K
7. South Is. & Stewart Is.	-46.50	-54.50	165.50	174.50	E	G	K
8. Tasmania	-37.50	-45.50	142.50	149.50	E	G	W
9. Ponta de Calcanhar	-2.50	-9.50	-37.50	-31.50	E	G	W
10. Mathematician's Seamounts	14.50	16.50	-112.50	-109.00	E	G	W
11. Hawaii	22.50	18.75	-160.50	-154.50	S	G	W
12. X-Mas Island	2.50	1.50	-158.00	-157.00	S	G	W
13. Emperor of Seamounts Chain (1)	31.75	36.00	170.50	173.50	E	G	W
14. Emperor of Seamounts Chain (2)	46.50	37.50	168.50	171.50	E	G	W
15. Cape Leeuwin	-32.50	-36.00	113.50	118.50	E	G	W
16. Wilke's Coast	-63.50	-66.50	129.50	140.50	E	W	W
17. Mascaren Plateau	-7.50	-18.50	58.50	63.50	E	G	W
18. Princess Martha Coast	-69.00	-72.50	-15.50	-0.50	E	W	W
19. Gambia	17.50	10.50	-20.50	-13.50	E	G	W
20. Rockall Bank	59.50	55.50	-17.50	-12.50	E	G	K
21. Faeroe Island	63.50	60.50	-10.50	-4.50	E	G	W
22. Great Meteor Seamount	35.00	29.50	-27.00	-31.50	E	G	W
23. Flemish Cap, Newf. Seamounts	49.00	45.50	-48.50	-43.00	E	G	K
24. Cape Palmas	2.50	6.50	-10.50	-4.50	E	G	W
25. Victoria Land	-65.50	-75.00	154.50	177.50	E	W	W

Notes.

* E. ETOPO5 Bathymetry Database
S· Scripps Bathymetry Database
W WOA 1 Sound Speed Database
G GDEM Sound Speed Database

\+ WKB Used for all regions at 10 Hz
W = WKB for all seasons at 50 Hz
K = Kraken for some seasons at 50 Hz

Table 4(Part 2): High Resolution Areas

Grid Name and Number	Latitude (N)		Longitude (E)		Data*		Model+
26. Tuamotu	-14.00	-18.50	-148.50	-140.50	S	G	W
27.1. Fiji (1)	-16.00	-19.50	176.75	179.50	S	G	W
27.2. Fiji (2)	-16.00	-19.50	-179.75	-178.00	S	G	W
28. Carnegie Ridge & Isla Isabela	1.50	-2.5	-92.50	-86.5	S	G	W
29. Johnston Atoll	16.25	17.25	-169.75	-168.5	S	G	W
30. Hawaiian Ridge (1)	29.5	24.50	-179.5	-169.50	S	G	W
31. Nova Trough	6.50	3.50	-162.75	-159.25	E	G	W
32. South Georgia Island	-53.00	-56.50	-43.50	-34.50	E	G	K
33. North Island	-36.50	-38.50	175.50	179.75	S	G	W
34. New Caledonia	-17.75	-23.50	162.50	169.5	S	G	W
35. Solomon Islands	-5.50	-11.50	153.50	162.50	S	G	W
36. Kuril Islands	46.50	42.50	145.50	151.50	E	G	K
37. Kamchatka Peninsula	51.50	46.75	151.75	156.50	E	G	K
38. Mascarene Islands	-21.50	-18.50	54.50	58.50	S	G	W
39. Mid-Atlantic Ridge	36.50	40.00	-34.50	-24.00	S	G	W
40. South Orkney	-60.00	-62.50	-48.50	-41.00	E	W	W
41. Crozet & Prince Edward Islands	-44.00	-47.50	37.50	52.50	E	W	W
42. Mill's Bank	-46.75	-47.75	147.50	149.00	E	G	W
43. Hawaiian Ridge (2)	22.50	26.00	-169.75	-160.75	E	G	W
44. Tahiti	-18.50	-16.00	-152.50	-149.00	S	G	W
45. Iles Marquises	-10.50	-7.50	-141.50	-138.5	S	G	W
46. Chatham Island	-42.50	-45.50	-179.75	-174.50	S	G	W
47. Samoa	-14.50	-11.50	-179.75	-171.00	S	G	W
48. Mid-Pacific Seamounts	17.50	20.00	166.25	167.75	E	G	W
49. Marshall Islands (1)	9.50	12.00	160.50	162.50	E	G	W
50. Marshall Islands (2)	5.50	12.50	164.50	172.25	E	G	W
51. Gilbert Islands	-3.5	3.50	172.50	177.50	S	G	W

Notes.

* E ETOPO5 Bathymetry Database
S· Scripps Bathymetry Database
W. WOA 1 Sound Speed Database
G· GDEM Sound Speed Database

\+ WKB Used for all regions at 10 Hz
W = WKB, K = Kraken for 50 Hz

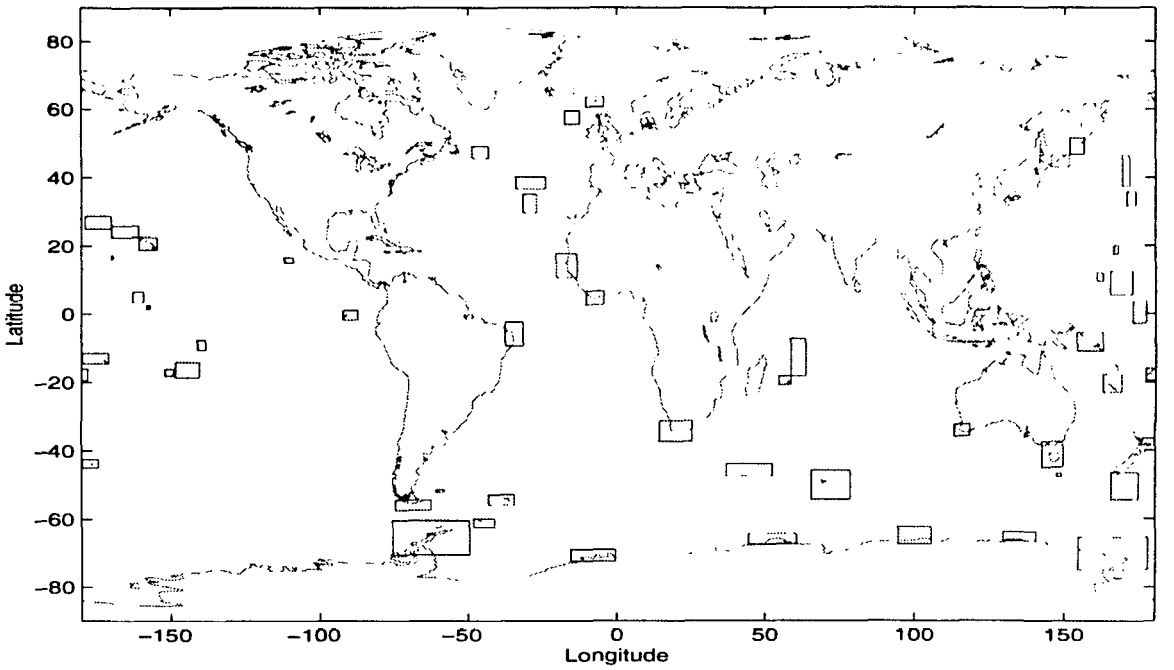

Figure 3: Regions for High-Resolution Modal Property Grids

First, world-wide grids were generated for mode 1 at 10 Hz in the Winter. Figures 4 - 7 show the differences between WKB and Kraken for the phase speed, group speed, attenuation and group speed variance grids. The differences between Kraken and WKB for both phase and group speed were less than 1 m/sec for the vast majority of the world. The differences exceeded 5 m/sec in isolated regions, including the Mediterranean Sea, the Red Sea, the Falkland Islands and off the eastern coast of Florida. In other regions, such as the Barents Sea, the eastern shore of Greenland and the Hudson Bay, the difference was between 1 and 5 m/sec. In these regions, WKB consistently exhibited higher phase speeds and lower group speeds than Kraken. The difference in attenuation, as measured as a per cent difference of the logarithm of attenuation, was also good world-wide with differences exceeding 1 per cent only in the regions previously mentioned for phase and group speed. Kraken showed slightly more attenuation in these regions. The difference in group speed variance was essentially zero throughout the world. As shown in the figures, most of these differences will have minimal impact on the grid accuracy, since either the magnitude of the approximation error is small, the error is over a very small region (e.g. near the Falkland Islands) or the error is in a location where raypaths from the IMS stations are unlikely to enter (e.g. the region between the Falklands and South America and the Mediterranean Sea).

Comparisons between WKB and Kraken were also performed on a high-resolution region (Hawaii) using 5 minute resolution for mode 1 at 10 Hz and 50 Hz. As indicated by Figures 8 - 10, the difference between the two models in the phase speed, group speed, and attenuation grids for the 10 Hz case was very small for the majority of the region. The isolated cells where the difference between WKB and Kraken in the phase and group

speeds exceeded 5 m/sec occurred at places where Kraken failed to produce a mode function. As seen in the figures, these areas are extremely shallow, in areas where significant raypaths are unlikely to traverse. The phase and group speed differences were less than 1 m/sec elsewhere. The percent difference in the logarithm of attenuation was also small, exceeding 1 per cent only at isolated cells. The differences between the grids generated by WKB and Kraken for the 50 Hz case were even less and are not shown here.

Figures 11 and 12 show phase speed and attenuation as a function of bottom depth (250 - 3000 m) for WKB and Kraken for mode 1 at 10 Hz and 50 Hz. The agreement is excellent in all cases considered except for a bottom depth of 250 m at 10 Hz where WKB fails to produce a proper mode structure. For the 50 Hz case, the attenuation for both Kraken and WKB is essentially zero for depths greater than 2000 m.

Comparisons between WKB and Kraken were also made for higher modes. Figures 13 and 14 show results for a bottom depth of 5000 m at 10 Hz for modes 1-15. The agreement for phase speed and attenuation is very good for all modes. The agreement in the imaginary portion of the wavenumber and the value of the mode function at the bottom is good for the first 12 modes and the first 11 modes respectively. Comparisons between WKB and Kraken for the first 15 modes are also shown for a bottom depth of 5000 m at 50 Hz in Figures 15 and 16. While there is essentially no difference in phase speed between the two models for any of the modes, there are some differences in the imaginary portion of the wave number, the attenuation, and the value of the mode function at the bottom for modes 3, 8 and 13.

Due to the small magnitude of the differences in the grids generated by WKB and Kraken for mode 1, and given the substantial savings in execution time, WKB was selected as the acoustic model to generate all of the modal grids. However, during the generation and review of the 50 Hz grids, several areas where noted where WKB had difficulties converging. The convergence problems were small (on the order of 2-5 m/s), seasonally dependent and were most likely due to the presence of several minima in the sound speed profiles. Instead of modifying the WKB search procedure for these special cases, we opted to use Kraken for these regions and the seasons where problems were noted (for 50 Hz only). These regions are identified with a "K" in the right-most column of Table 4.

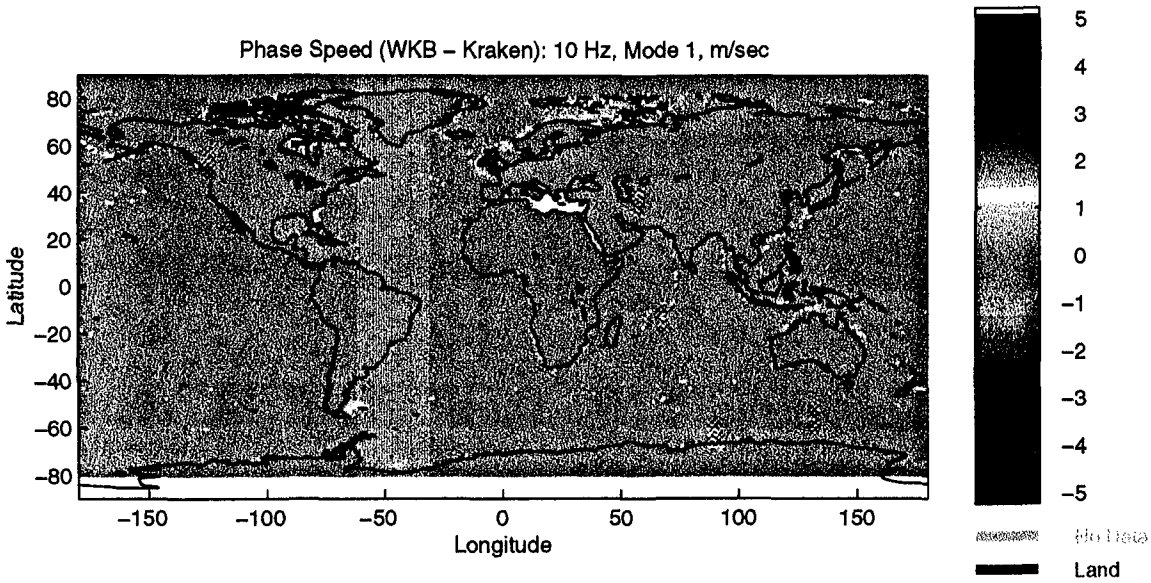

Figure 4: Phase Speed Difference (WKB-Kraken) for Mode 1 at 10 Hz

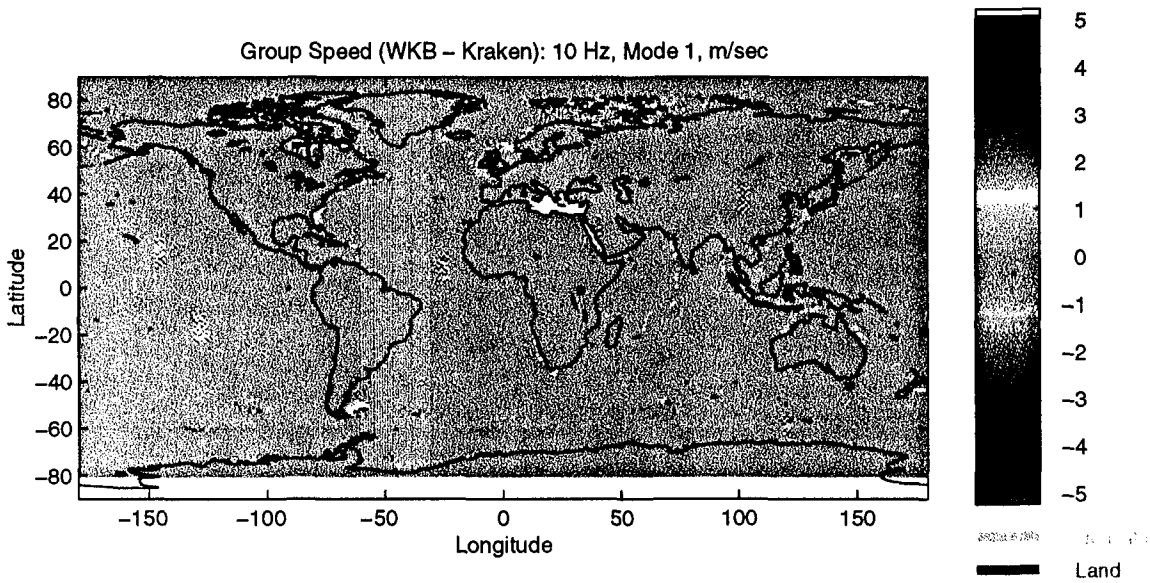

Figure 5: Group Speed Difference (WKB-Kraken) for Mode 1 at 10 Hz

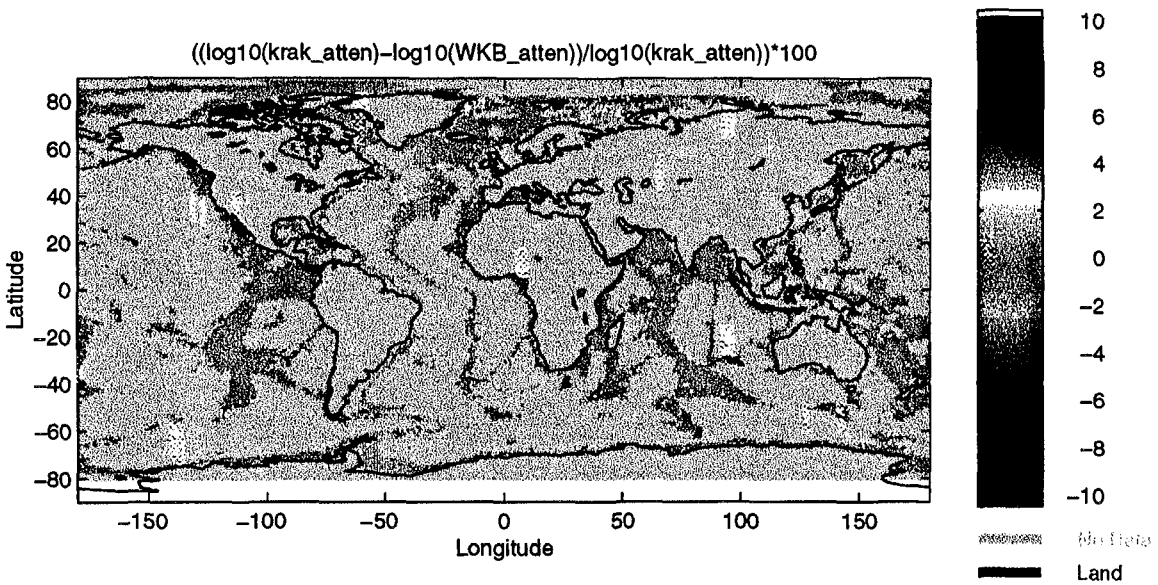

Figure 6: Percent Difference in Modal Attenuation (WKB-Kraken) for Mode 1 at 10 Hz

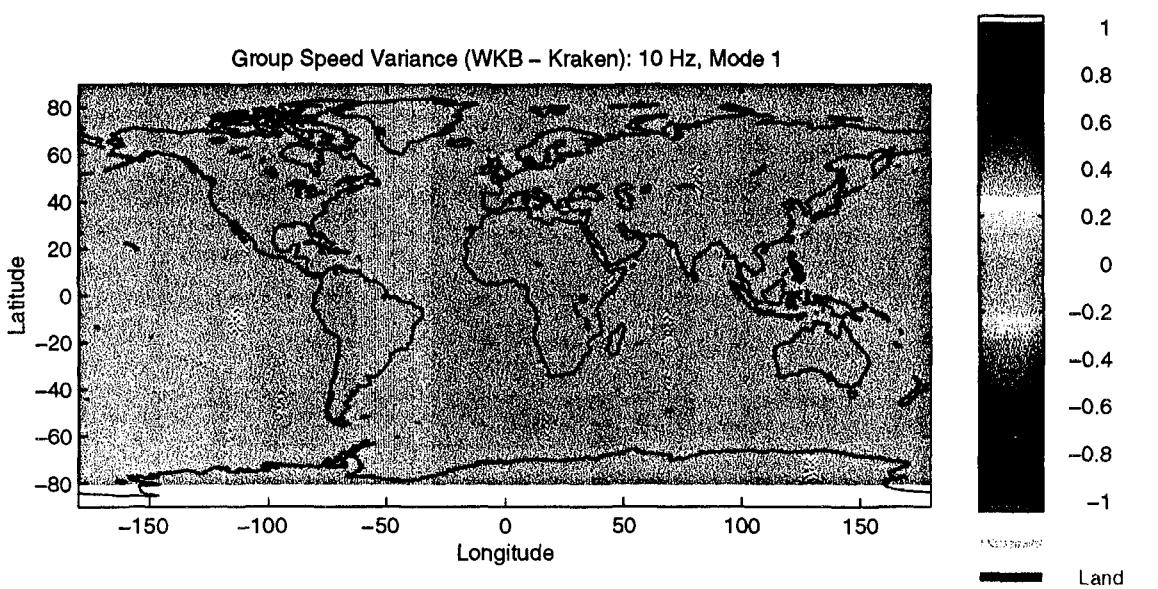

Figure 7: Difference in Modal Slowness Variance (WKB-Kraken) for Mode 1 at 10 Hz

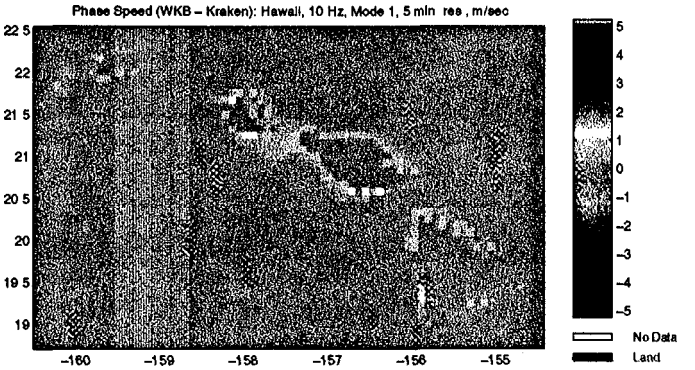

Figure 8: Phase Speed Difference (WKB-Kraken) for Mode 1 at 10 Hz

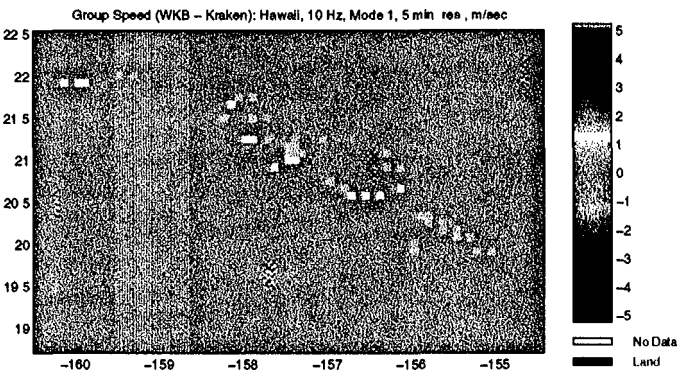

Figure 9: Group Speed Difference (WKB-Kraken) for Mode 1 at 10 Hz

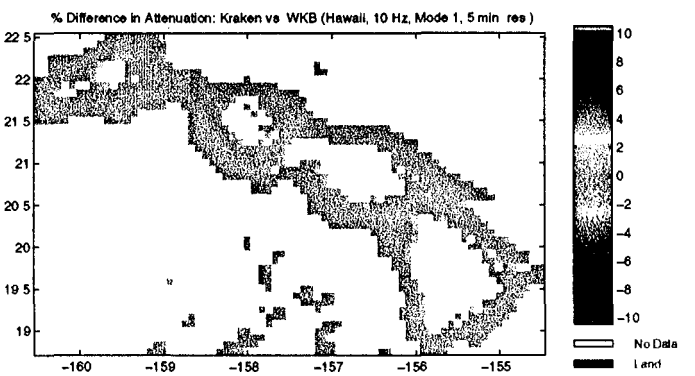

Figure 10: Percent Attenuation Difference (WKB-Kraken) for Mode 1 at 10 Hz

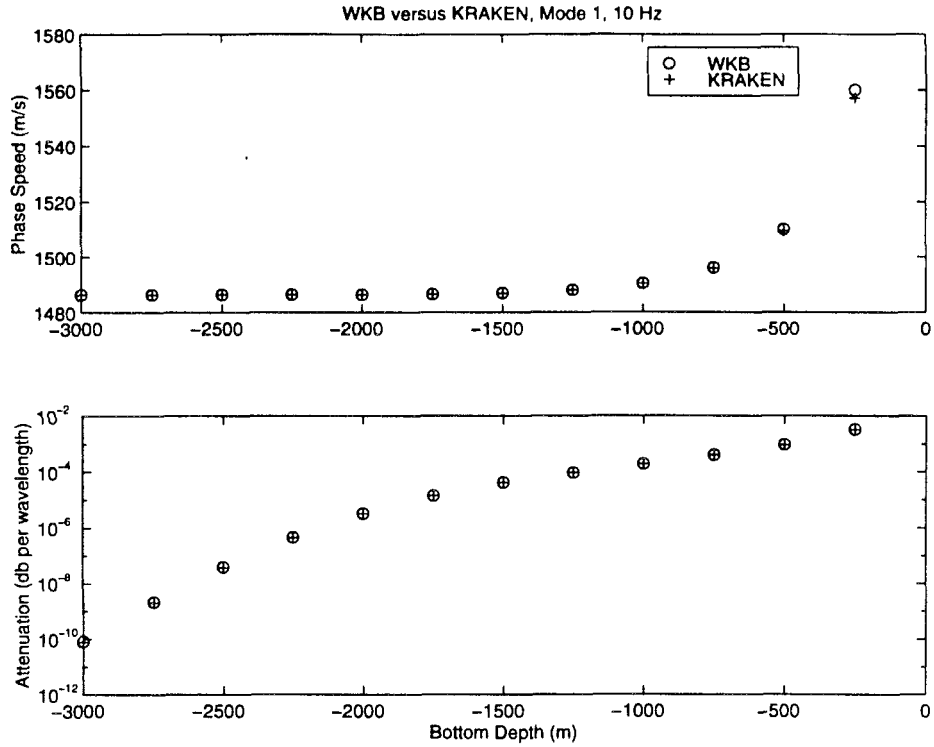

Figure 11: Phase Speed and Attenuation vs Bottom Depth (10 Hz, Mode 1)

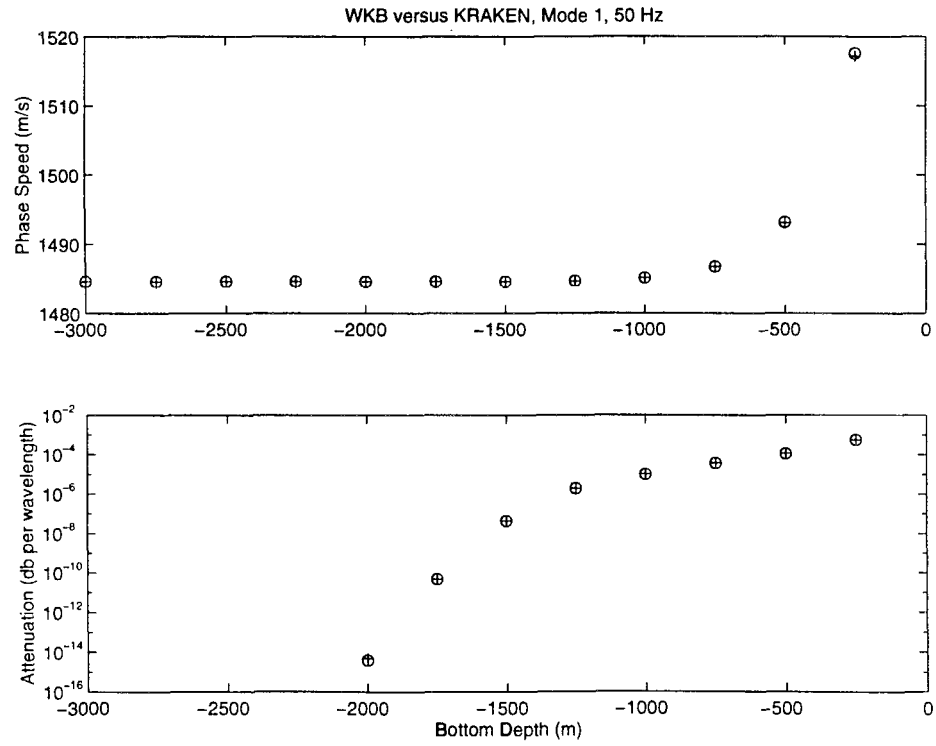

Figure 12: Phase Speed and Attenuation vs Bottom Depth (10 Hz, Mode 1)

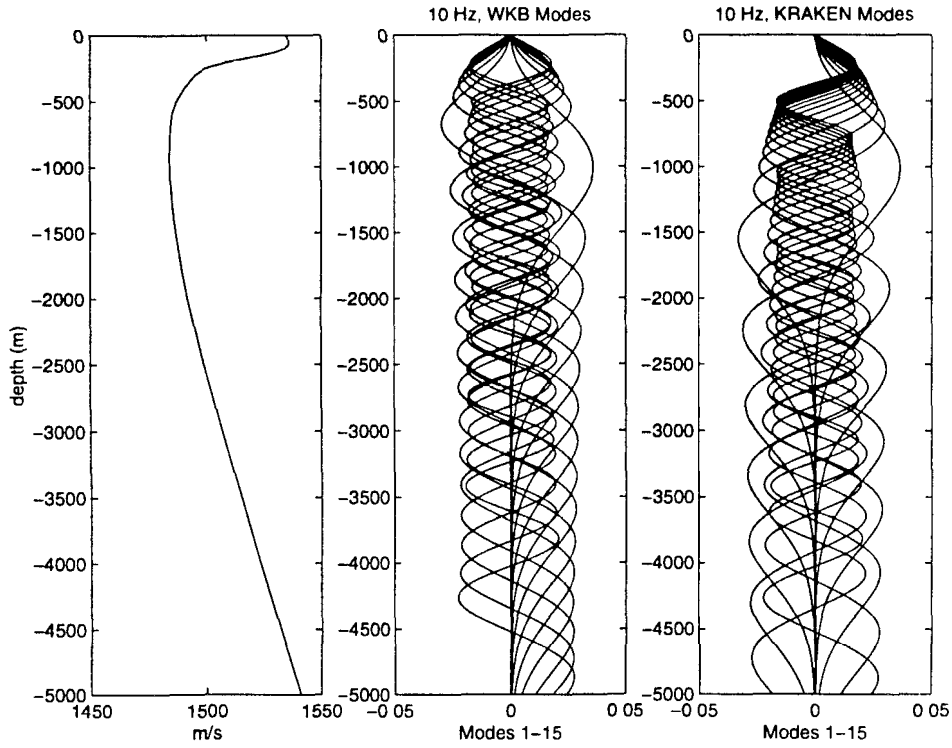

Figure 13: Mode Functions at 10 Hz for WKB and Kraken

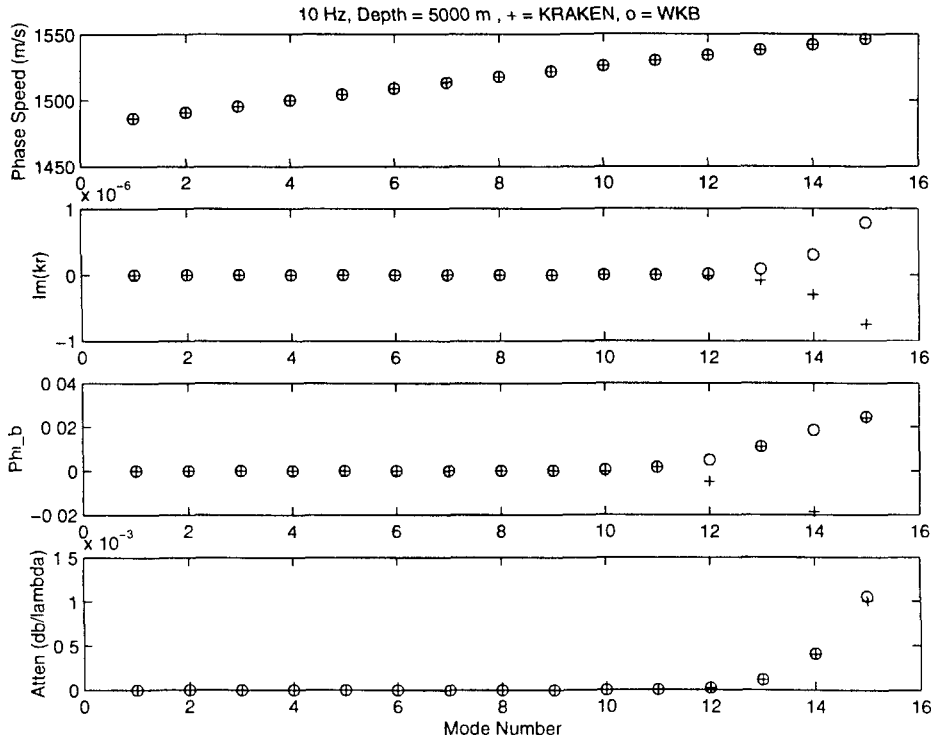

Figure 14: Phase Speed and Attenuation for Higher Order Modes (10 Hz)

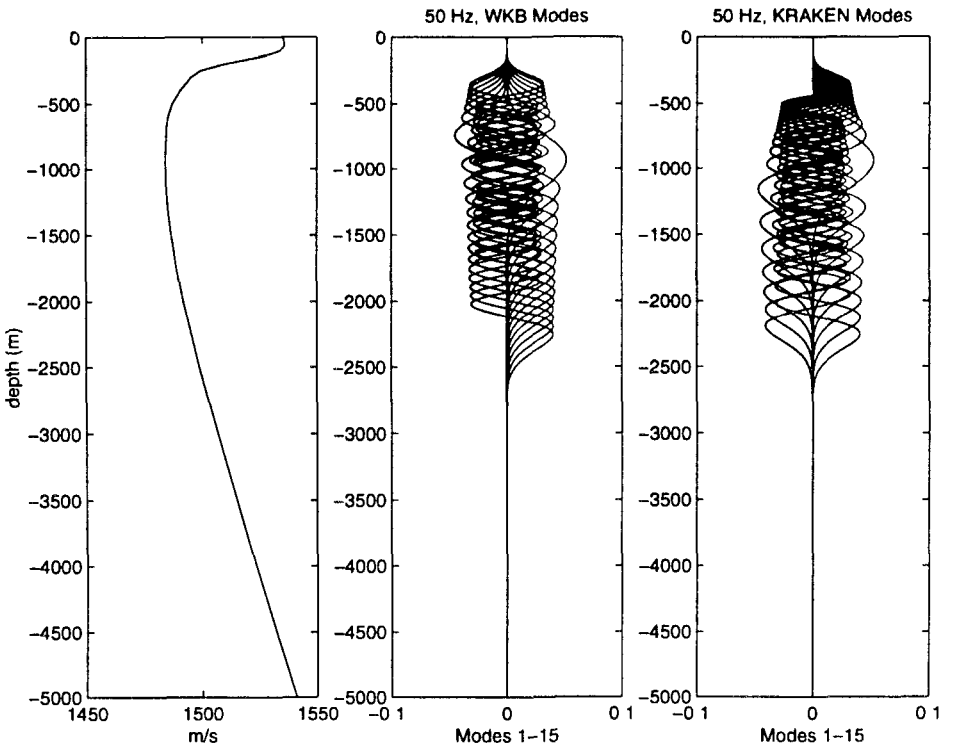

Figure 15: Mode Functions at 50 Hz for WKB and Kraken

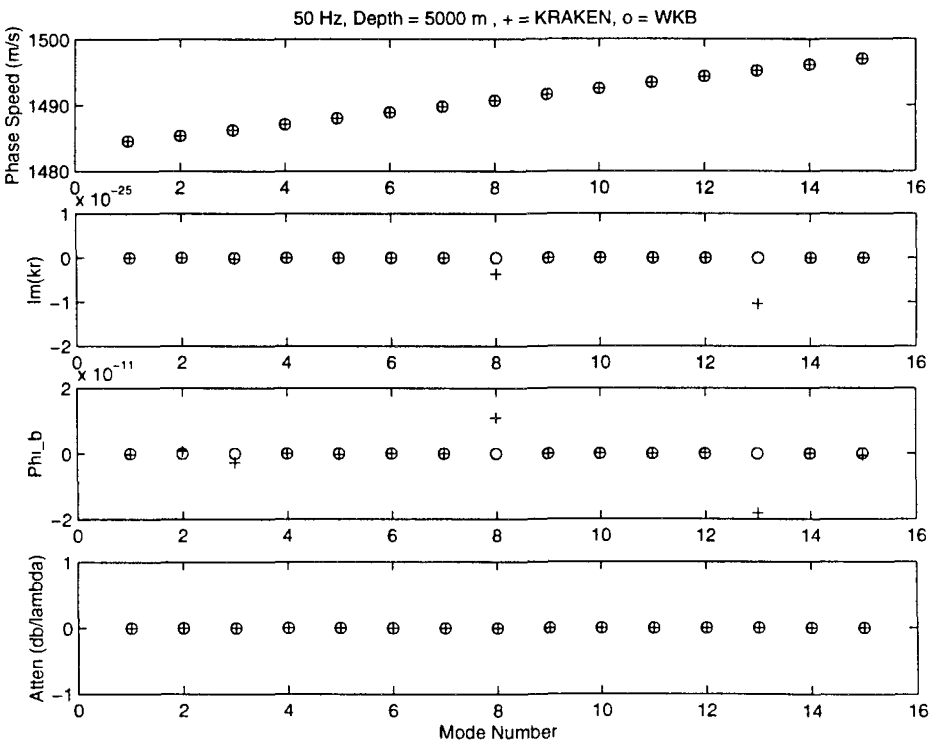

Figure 16: Phase Speed and Attenuation for Higher Order Modes (50 Hz)

2.3.3 Environmental Databases

Sound Speed

The two primary sound speed databases included in HydroCAM are the World Ocean Atlas (WOA) Analyzed database from NOAA [5] and the Generalized Digital Environmental Model (GDEM) from the Naval Oceanographic Office [6]. Since the WOA is global in coverage, it will be used in generating the world-wide grids. GDEM provides coverage north of 40° South in the Indian Ocean and north of 60° South elsewhere but has the advantage of better resolution (0.5° vs. 1° for WOA). A comparison of the modal grids was made using WOA and GDEM sound speed profiles for the high-resolution areas which had GDEM profiles. In some instances, the phase and group speed grids generated with WOA exhibited uncharacteristically low levels near coastal regions; due to interpolation of deep water profiles into very shallow regions. The grids generated with GDEM showed a more realistic behavior since GDEM's finer resolution results in better interpolated profiles. An example of this artifact is shown in Figures 17 and 18 which details the differences in the phase and group speeds between the two databases for the Hawaii region. GDEM derived phase and group speeds were more than 5 m/sec larger than WOA near the eastern and southern shore of the main island. Also, the difference in the logarithm of the attenuation exceeded 10 percent in the these same areas, as shown in Figure 19. For these reasons, GDEM was used for all high resolution areas where coverage was available (42 of the 51 high-resolution regions).

It is significant to note that the differences in the modal grids when comparing the two acoustic mode models (Figures 8-10) are less than the differences in the grids when comparing the two sound speed databases (Figures 17-19). This suggests that the selection of appropriate environmental databases (and an accurate profile interpolation procedure) weighs more heavily in the end results than the choice of mode model.

Sound Speed Standard Deviation

The only available database with sound speed standard deviation profiles is the WOA Analyzed 5 degree resolution database. This database, which includes seasonal and annual average profiles, will be used in the generation of the group speed variance grids. Since the annual average standard deviation database provides better world-wide coverage than the seasonal databases, and the differences between the modal slowness variances calculated with the seasonal databases was determined to be minimal, the annual average database will be used to generate both the world-wide and high-resolution grids. Since the database is provided at 5 degree resolution and most of the high-resolution grids are regions contained in one or two WOA5 cells, the high-resolution slowness variance grids will not be used in the travel time variance calculations.

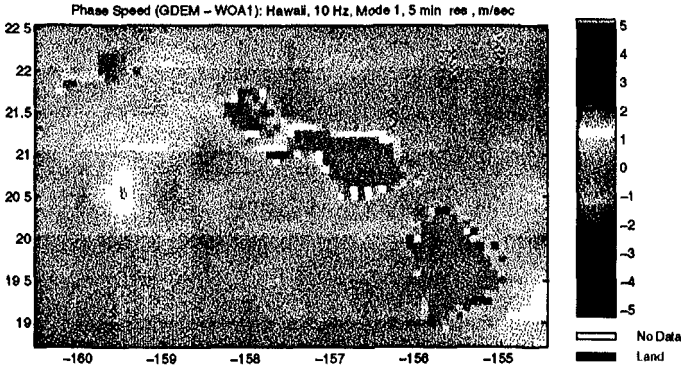

Figure 17: Phase Speed Difference (GDEM - WOA 1) for Mode 1, 10 Hz

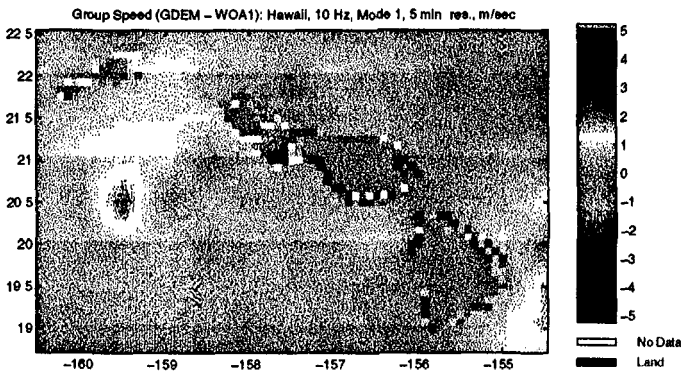

Figure 18: Group Speed Difference (GDEM - WOA 1) for Mode 1, 10 Hz

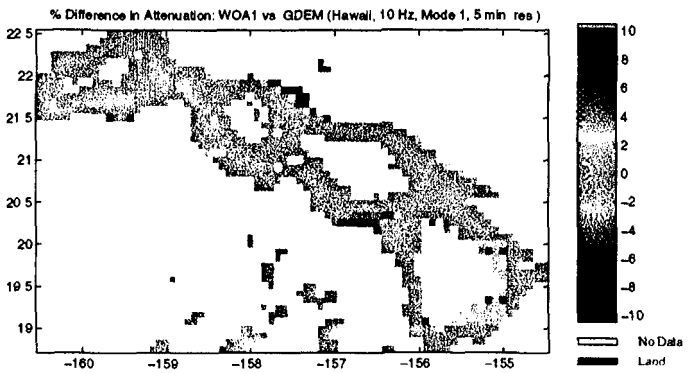

Figure 19: Modal Attenuation Difference (GDEM - WOA 1) for Mode 1, 10 Hz

Bathymetry

The primary bathymetry database used in HydroCAM is ETOPO5 (Earth Topography, 5 minute resolution). It is well known that ETOPO5 has significant artifacts in some coastal areas [7], does not include several islands in the South Pacific and Indian Oceans (such as Easter Island and Crozet), and in general suffers from a lack of ship-based measurements in the southern hemisphere. Recently, a bathymetry database from the Scripps Institute of Oceanography [8], which uses satellite derived gravity measurements to interpolate bathymetry from ship-based measurements, was incorporated into HydroCAM and analyzed for its potential use. The Scripps database is provided on a Mercator grid, with samples every 2 minutes in longitude. Sampling in latitude varies, with the largest spacing occurring every 2 minutes at the equator.

Bathymetry from ETOPO5 and the Scripps database was compared for each of the 51 high resolution areas. To perform this comparison, the function *image2latlon*, provided with the Generic Mapping Tools (GMT) software, was used to interpolate the Scripps bathymetry onto an even lat/lon grid with 2 minute resolution. This function is also used by the HydroCAM software to access the bathymetry data. The data from both databases was also compared to GEBCO oceanographic charts [9]. In 18 of the high-resolution regions, the Scripps database clearly provided a more accurate representation than ETOPO5 and will be used in the modal grid generation procedure. For regions exhibiting minor discrepancies between the two databases, ETOPO5 will be used.

In a number of the other high resolution regions the Scripps database provides a more accurate representation in certain portions of the region, but exhibits anomalous land masses which could not be verified by oceanographic charts (eg. near Tasmania and Crozet Island as shown in Figure 20). Another example is the substantial discrepancies in the land masses between the two databases in several coastal Antarctica regions (eg. Palmerland and Queen Mary Coast as shown in Figure 21). A possible explanation for this is that thick ice cover may be interpreted by gravity measurements as shallower elevations, resulting in the location of land masses in the Scripps database that is dependent on the extent of the ice cover at time of year that the measurements were taken. These artifacts may also be due to the interpolation procedure contained in *image2latlon*. This type of artifact would have particular impact in the Queen Mary Coast area as this area was selected because a number of stations have ray paths that graze the coastline. Artificial land masses around the coast in this area would cause additional blockage to occur. For high-resolution areas with either the anomalous land masses and/or ice cover regions, the ETOPO5 database will be used.

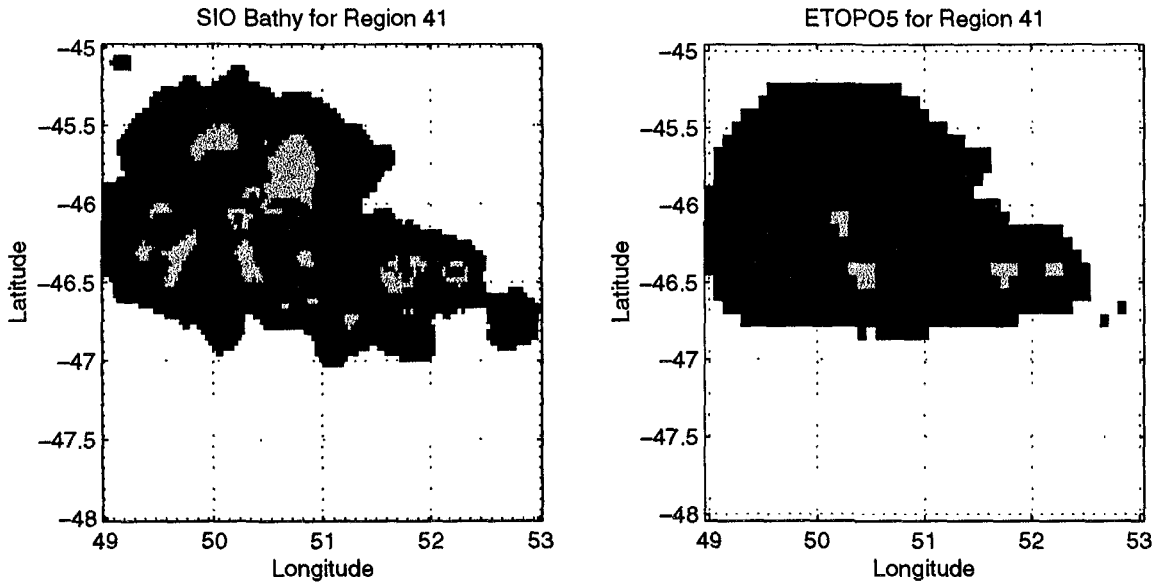

Figure 20: Scripps and ETOPO5 Bathymetry for Crozet (Region #41)

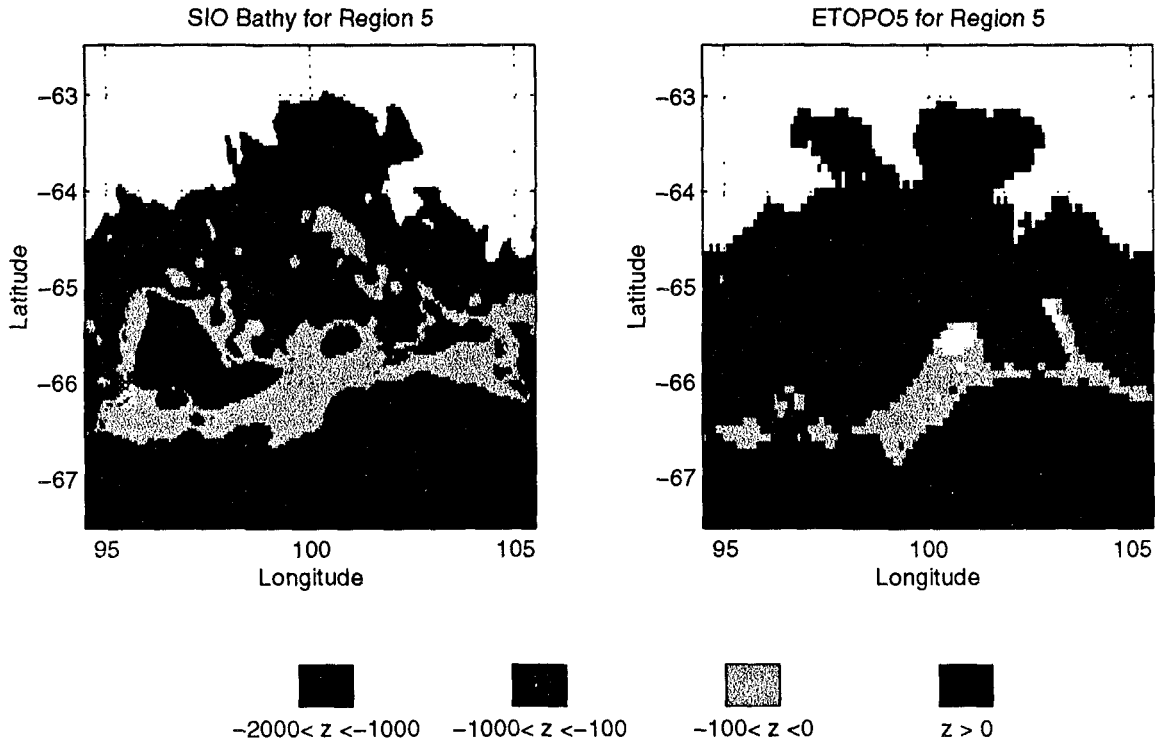

Figure 21: Scripps and ETOPO5 Bathymetry for Queen Mary Coast (Region #5)

Bottom Model

The limited amount of unclassified data regarding the bottom interaction of sound transmission in the ocean prohibits the implementation of a detailed geoacoustic model to account for bottom loss in each area. Thus, a simple fluid half space model which assumes constant bottom sound speed, density and attenuation is used to model the effects of bottom loss. A similar approach to bottom loss was used in [10] to model transmission loss from Heard Island signals received near the Gulf Stream. The values for the three bottom parameters which will be used for the grid generation, as indicated in Table 3, were derived from the Heard Island parameters in [10], which were based on results in [11] and [12].

A different set of bottom loss parameters which were derived from a Navy standard bottom loss database was also used to generate world-wide modal grids for purposes of comparison. Figures 22 - 24 summarize the differences in phase speed, group speed and attenuation between these two sets of parameters. Except for isolated grid cells, the phase speed difference was essentially zero world-wide. Phase speeds based on parameters from the Heard Island experiment were less than those based on the Navy standard model by about 1 m/sec in a few regions such as the Barents Sea, the coast of Greenland and the coast of Florida. The same comments apply to group speed, except the values were larger using parameters derived from the Heard Island experiment in the same regions. The difference in the logarithm of the attenuation for the two sets of parameters was less than 5 per cent for the vast majority of the world.

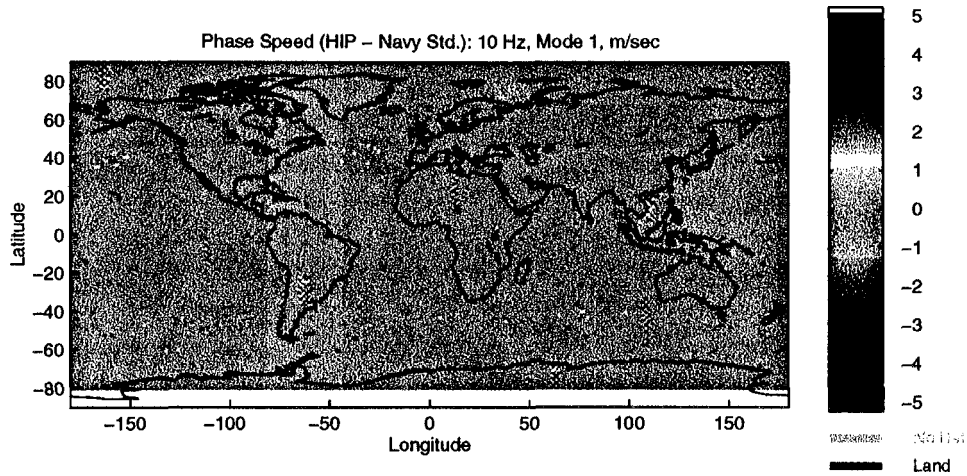

Figure 22: Phase Speed Difference (Heard Island Bottom Model vs Navy Standard)

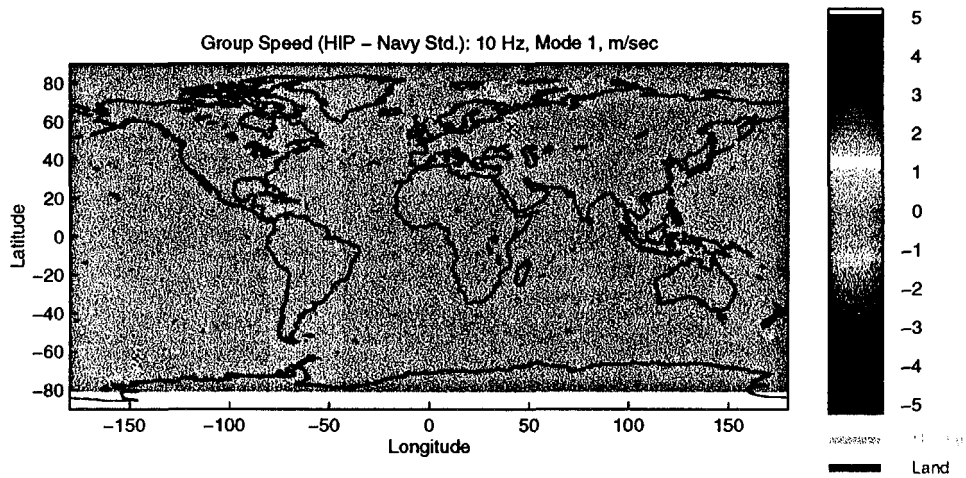

Figure 23: Group Speed Difference (Heard Island Bottom Model vs Navy Standard)

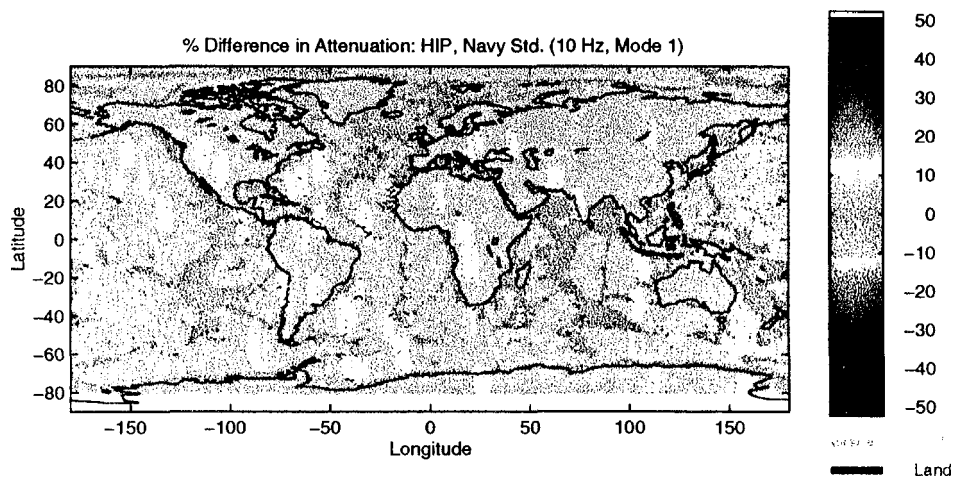

Figure 24: Modal Attenuation Difference (Heard Island Bottom Model vs Navy Standard)

2.3.4 Grid Parameters

A set of modal grids for the world-wide and each of the 51 high-resolution areas were generated using mode 1 at 10 Hz and 50 Hz for Winter, Spring, Summer and Fall. Resolution for the world-wide grids was 1°. The effects of different resolutions for the high-resolution grids was analyzed by shooting refracted rays from Crozet Island around the Cape of Good Hope and examining the differences in the rays paths. Sets of rays spaced .25° apart in azimuth were shot into a high-resolution modal grid near the Cape of Good Hope using resolutions of 30', 15' and 5'. This is shown in Figures 25 - 27. The rays paths were markedly different inside of the high-resolution region, as indicated in Figures 28-30. The differences in the maximum spread between the ends of the ray paths at the eastern seaboard of the U.S. for the three cases was significant. Based on these results and the assumption that finer resolution yields more accurate estimates, it was determined that a resolution of 5' should be used in the generation of the high-resolution grids.

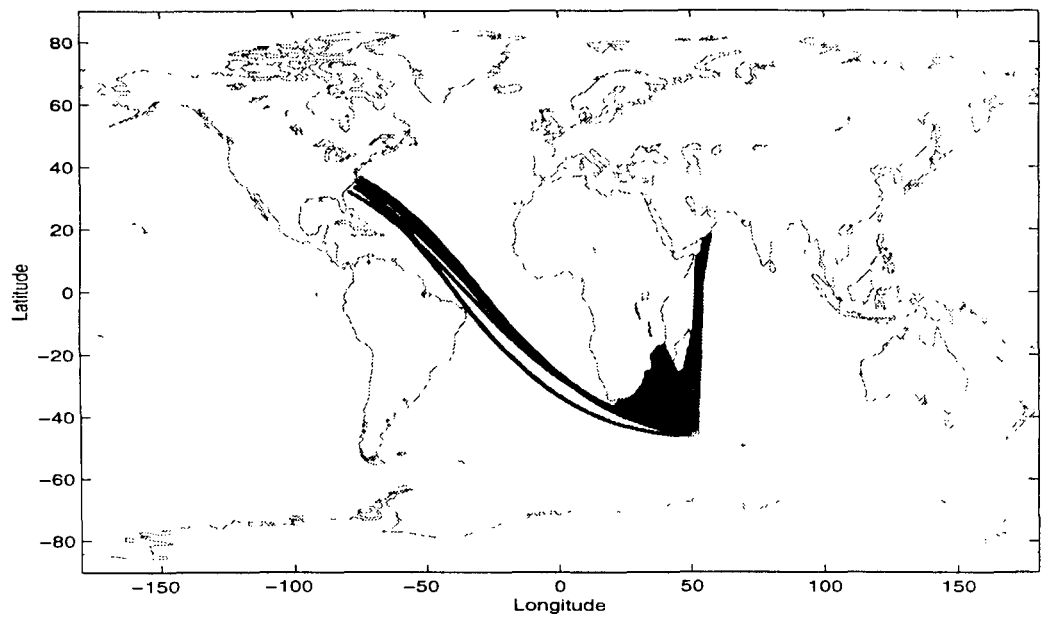

Figure 25: Refracted Rays with 30 Minute Resolution Phase Speed Data

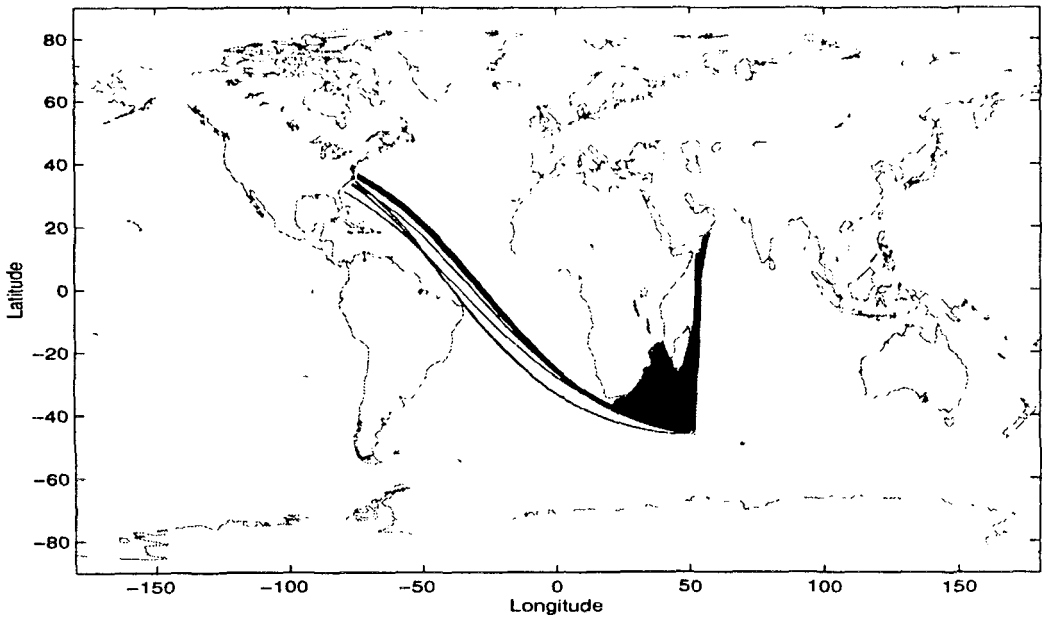

Figure 26: Refracted Rays with 15 Minute Resolution Phase Speed Data

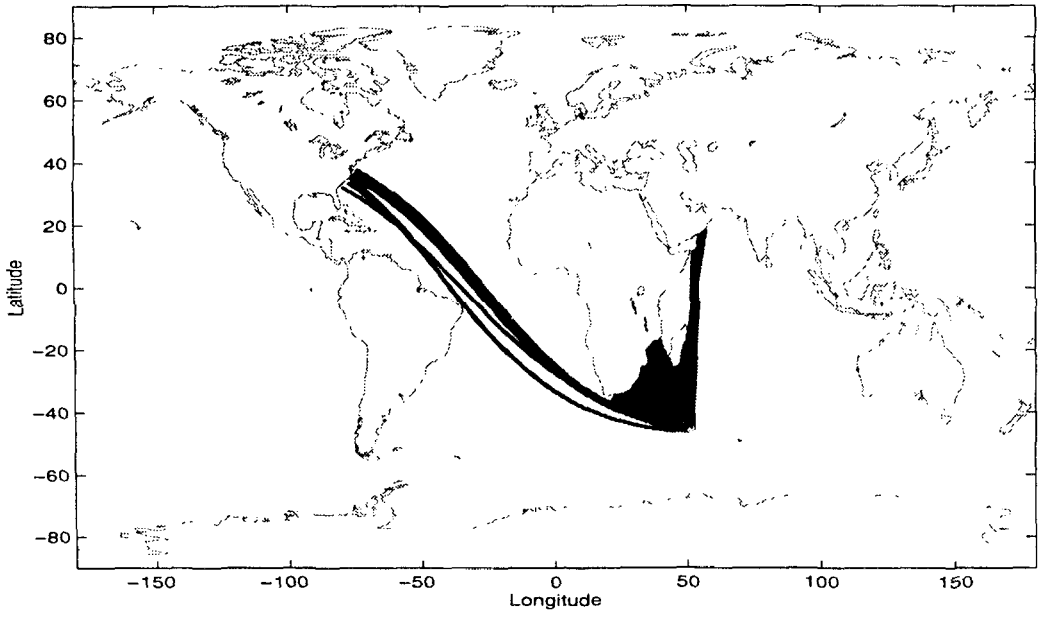

Figure 27: Refracted Rays with 5 Minute Resolution Phase Speed Data

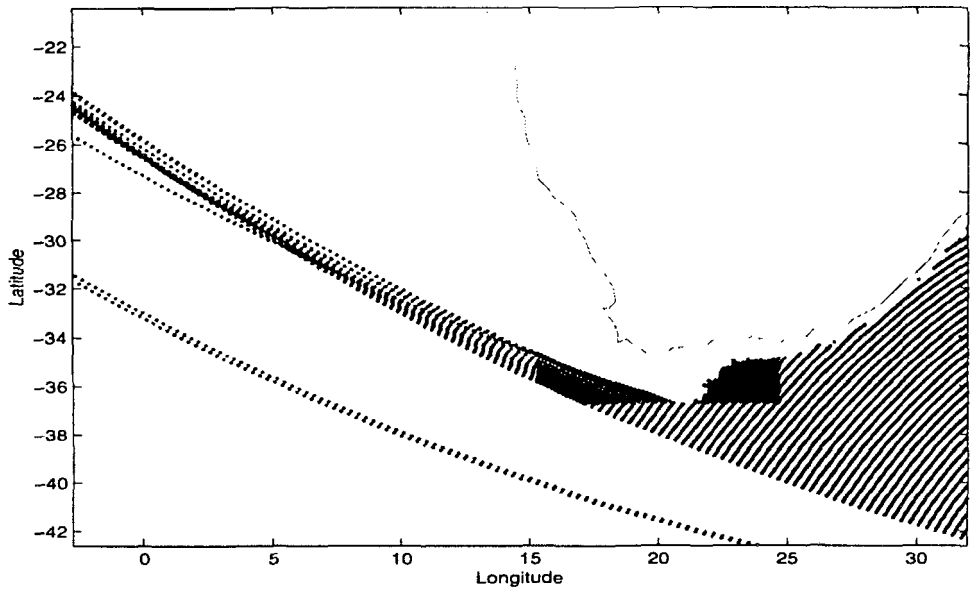

Figure 28: Refracted Rays with 30 Minute Resolution Phase Speed Data

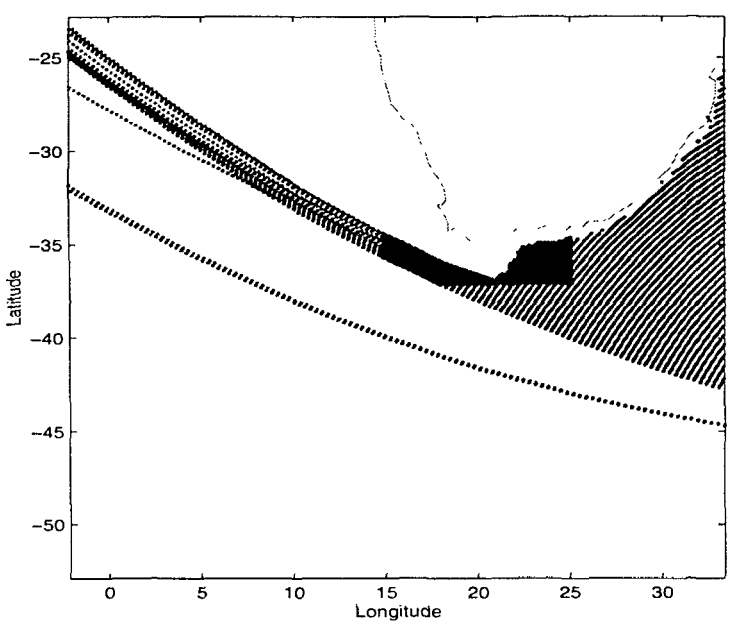

Figure 29: Refracted Rays with 15 Minute Resolution Phase Speed Data

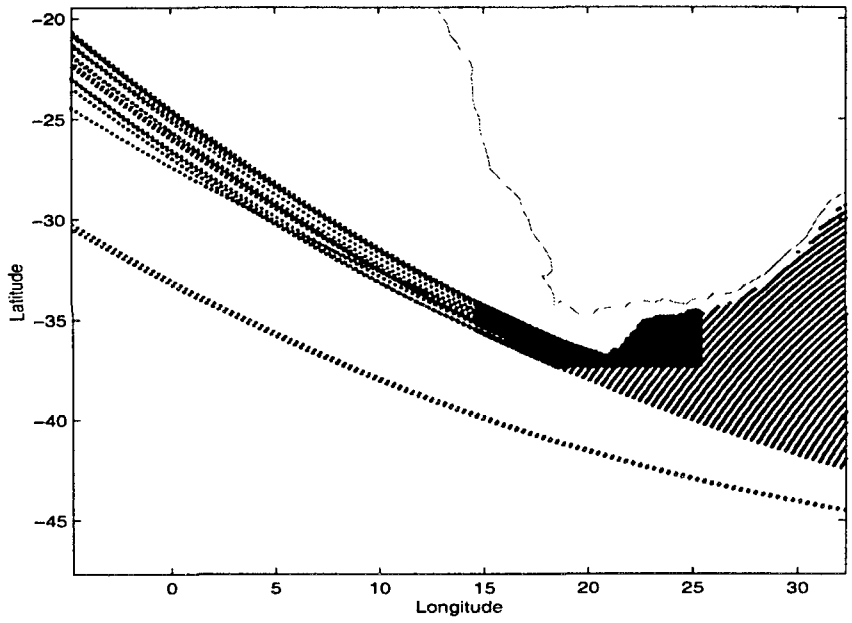

Figure 30: Refracted Rays with 5 Minute Resolution Phase Speed Data

2.4 Propagation Characteristic Grids:

Once the modal grids have been produced, a horizontal raytrace model is used to generate refracted paths for each of the receivers. Estimates for travel time, transmission loss, travel time standard deviation, range, and attenuation are computed along each ray path, which is spatially sampled every 0.25 degrees in azimuth with range steps of approximately 1 kilometer along each ray. The value for each path quantity is saved along each path every 30 kilometers. As a final step, the values for these five quantities along the refracted ray paths are then interpolated onto (uniformly spaced) 1 degree propagation characteristic grids.

Another option which was considered to generate the grids was to perform the propagation characteristic calculations directly to the source location grid points. This approach would have required finding the eigenrays from each receiver to the center of each cell in a world wide grid with 1 degree resolution. HydroCAM currently offers several models to perform this task, and each has several limitations [1,3]. The traditional approach is to iteratively perturb the ray's initial launch angle from the source until the refracted path passes through the receiver location to within a specified error tolerance. The drawbacks to this approach are that it is very computationally intensive, and that there is no guarantee that the method will converge for all situations, even when a large number of rays are generated.

An alternate approach is to perturb an initial path which actually connects the source and receiver until the travel time along the path is minimized. "Bending" the ray path to a specified error tolerance between successive iterations may result in a path which is close to the actual horizontally refracted eigenray. Although this approach has the advantage of always producing rays which pass through the center of each grid cell, it can also suffer from convergence problems. In addition, the "Bending" does not allow specification of which path is selected when multiple paths are present. In general, all approaches requiring path computations between fixed endpoints are computationally burdensome since the number of paths that need to be computed is proportional to the area covered. For these reasons, it was decided to generate refracted rays with uniform spacing in azimuth, and then interpolate the rays to grids uniformly spaced in latitude and longitude. In a sense, this approach re-uses the data in regions near the receiver to reduce the computations required for long raypaths.

2.4.1 Path Models

Most of the equations used to determine the path characteristics are contained in the *HydroCAM Users Guide [3].* However, increased interest by the US NDC in the path attenuation has caused several additional attenuation models to be added to HydroCAM. Since these models are not currently documented elsewhere, this section describes them.

General TL Models

The AFTAC version of the transmission loss equation is defined as

$$TL(R) = .22R + 10\log_{10}(.7 + 30R) + 10\log_{10}(\sin R) - 35.5 \quad (1)$$

where R denotes range measured in geographic degrees. The first term represents an absorption factor, the second is essentially cylindrical spreading and the third is a refocussing term. Two transmission loss models are currently supported by HydroCAM;

$$TL(r) = A + B\log_{10}(r) + Cr + I(r) \quad (2)$$

and

$$TL(r) = A + B\log_{10}\left[r\sin\left(\frac{r}{R_e}\right)\right] + Cr + I(r) \quad (3)$$

where r is range measured in kilometers, A, B, and C are constants, $I(R)$ is the integrated modal attenuation along the path and R_e is the radius of the earth in kilometers. Since it is unclear as to which model is generally acceptable to the hydroacoustic community, it was decided to provide both a range grid and a boundary attenuation (correction) grid, which includes only the $I(r)$ term. These two grids can be used in conjunction with any of the above transmission loss models to provide an estimate of transmission loss. The AFTAC model given by equation (1) will be incorporated into HydroCAM and delivered later this year.

In general, the $I(r)$ term can be thought to include

$$I(r) = L_B(r) + L_I(r) + L_S(r) + L_V(r) \quad (4)$$

where L_B includes losses due to the interaction with the ocean bottom (which are obtained by integrating the modal attenuation coefficient calculated by WKB or Kraken along the ray path), L_I is due to ice cover in polar regions, L_S is due to rough-surface attenuation and L_V is due to volume attenuation (absorption). Since L_V is normally accounted for using the C term in equations (2) or (3), and databases of the chemical factors affecting the term are not readily available, this term is set to zero in equation (4). At the start of this year's effort, L_I and L_S were not included in HydroCAM. The following two sections discuss these terms.

Ice Cover Attenuation

In polar regions where the ocean is covered with ice, the attenuation due to repeated surface interactions can dominate all other losses and result in the termination of acoustic paths. The magnitude of the loss is a complicated function of the ice cover characteristics (such as roughness, mean depth and ice composition), the frequency, and the grazing

angle. Since detailed databases of the relevant ice characteristics are not available (and the nature of the ice cover can change from year to year), a first-order model based on results from ONR experiments performed in the central Arctic is used [13]. These experiments directly measured the mode 1 ice cover attenuation as a function of frequency, as shown in Figure 31. The ice cover model employed in HydroCAM is a linear interpolation of the data shown in this figure between 10 Hz and 200 Hz.

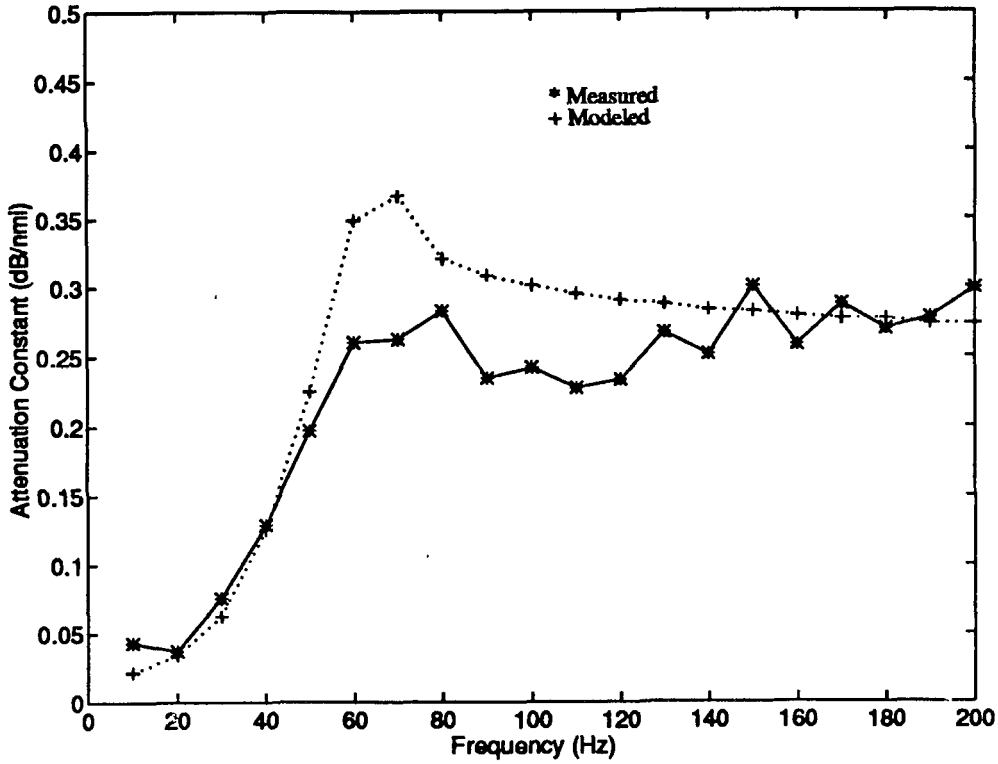

Figure 31: Measured and Modeled Attenuation Constant Vs Frequency from [13]

Now that the ice cover attenuation model has been selected, a choice for when and where to apply these losses must be made. The best available ice cover extent data seems to be the databases provided by the National Ice Center which are derived from the Defense Meteorological Satellite Program (DMSP). This database, which is updated monthly via the internet, contains ice cover extent for the northern and southern hemisphere on a polar stereographic grid. (See Figure 32 and Figure 33). This database has been translated to a single lat/lon grid and integrated into HydroCAM, such that when raypaths traverse an area where ice is present, the loss derived from Figure 31 is applied.

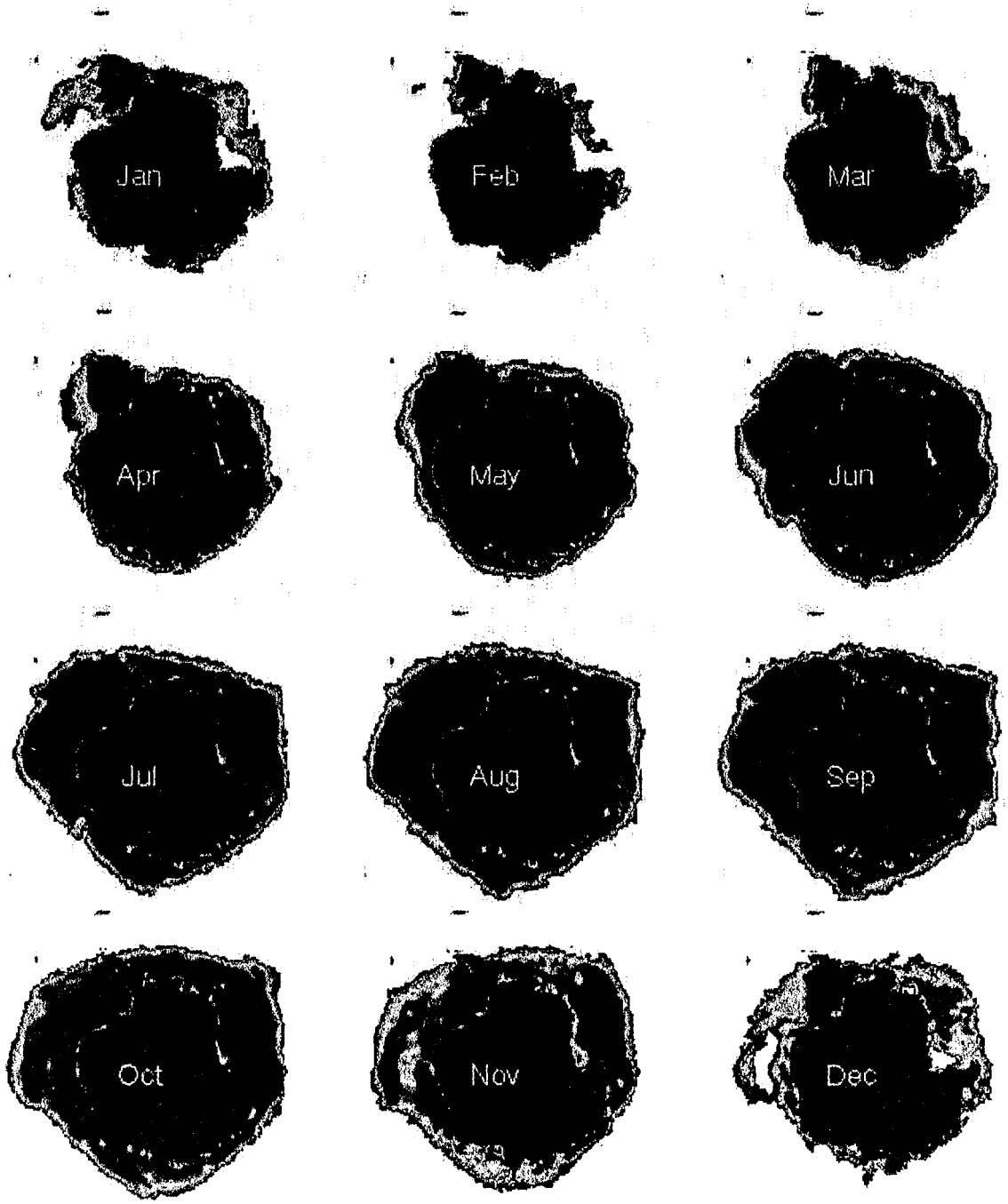

Figure 32: 1996 Southern Hemisphere Ice Cover Extent Measured by DMSP Satellite

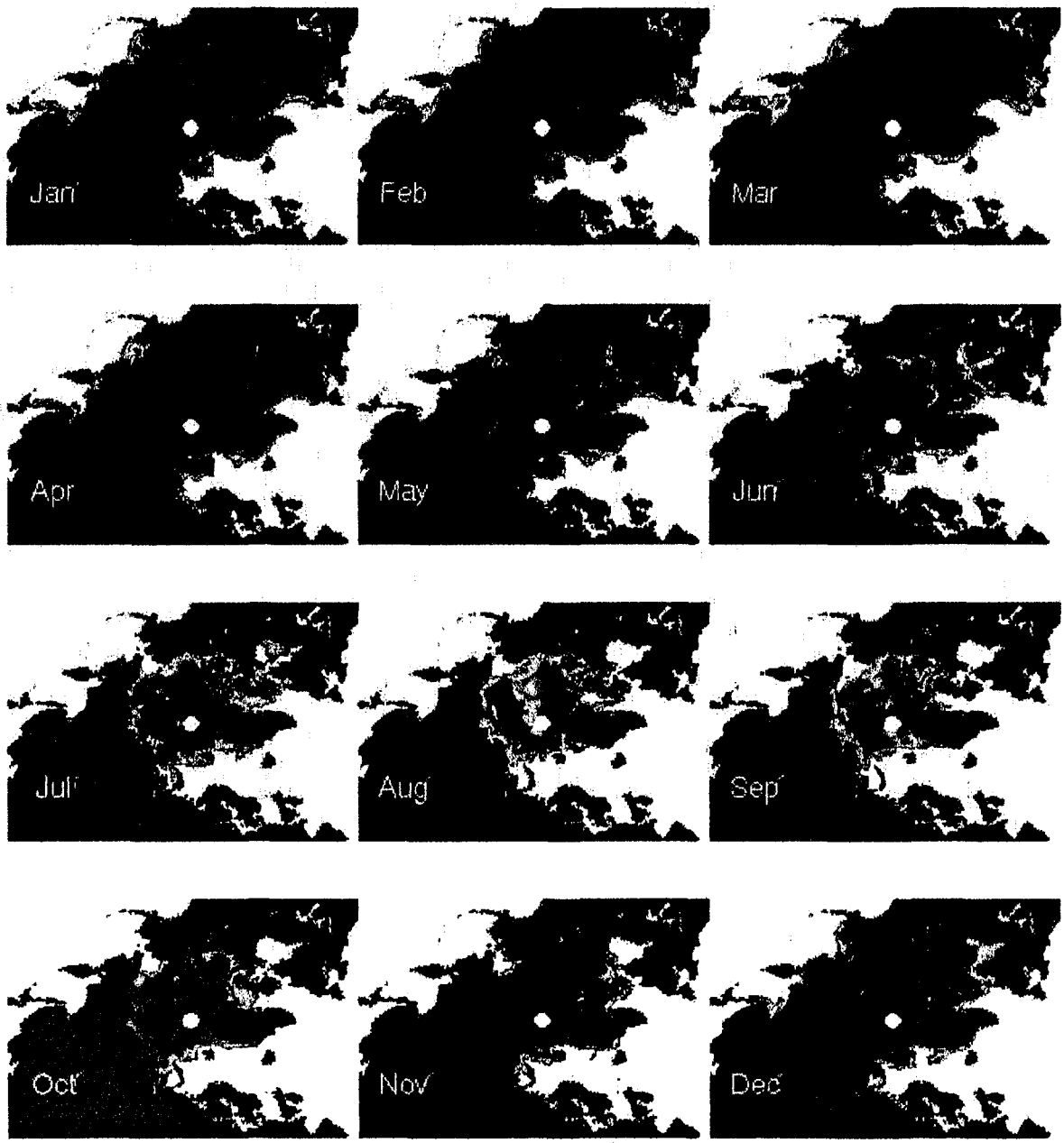

Figure 33: 1996 Northern Hemisphere Ice Cover Extent Measured by DMSP Satellite

Rough-Surface Attenuation

Several models for the rough-surface propagation loss were investigated as described in Appendix C. These models were used to calculate the magnitude of the loss for several wind speeds and several seasons. The results indicated that in mid-latitude and equatorial regions (which typically have a deep SOFAR channel), the surface loss is at least five orders of magnitude less than the ice cover and bottom losses already contained in HydroCAM. The loss is also at least an order of magnitude smaller at high latitudes, except under worst-case situations (such as local winter where the sound speed profile in high-latitude regions is strongly upward refracting *and* high 40 knot wind speeds are present). However, large areas where these conditions are present will be ice-covered, so that the rough-surface loss term would not need to be included. Due to the results of this study, we have decided not to incorporate the rough-surface model into the raytrace software at this time.

2.4.2 Interpolation Procedure

Several methods were considered to interpolate the refracted ray paths onto a grid. These included the four methods initially implemented in HydroCAM; 'quantize', 'average', 'nearest' and 'weighted'. These methods are described in detail in the *HydroCAM Users Guide [3].* Several tests were made using each of these methods comparing interpolated geodesic paths to geodesics on a uniformly spaced grid. The results using each of these four methods exhibited substantial errors and the methods were determined to be inadequate to accurately produce the propagation characteristic grids. Thus, an alternate approach to the interpolation procedure was considered.

The basic interpolation problem is to compute the values of travel time, travel time standard deviation, range and attenuation at the center of a grid cell from a set of points non-uniformly spaced throughout the cell. The non-uniform spacing of the points is primarily a result of the radial sampling of the ray paths shot from a station location. This sampling is then complicated by the ellipsoidal nature of the earth, and the effects of horizontal refraction, multipath and blockage from land masses. Of the quantities to be computed, travel time is the most difficult, since we will require accuracies on the order of 1 second (out of 10000 seconds). Under the first order assumption that the travel time varies linearly with distance along a ray path, a reasonable approach is to perform a least mean squares estimate to a plane containing the points in the geographic cell. Here, the x- and y-coordinates of the plane correspond to the longitude and latitude of the cell points, and the z-coordinate corresponds to travel time (or travel time standard deviation, range, attenuation, etc.). Once the equation of the plane has been determined, the z-coordinate of the cell center is readily computed given its latitude and longitude.

Several tests were performed to check the accuracy of this least squares approach. First, travel time, transmission loss, and travel time standard deviation grids interpolated using

geodesic paths from Ascension Island were compared to geodesics generated on uniformly spaced grids. The results for travel time are shown in Figure 34 and the errors for all three propagation quantities are summarized in Table 5. The agreement between the grid data and the interpolated path data was very good throughout the world. The average travel time error was 0.1103 seconds and the average transmission loss error was .0220 dB. The maximum error in travel time (6.1719 seconds) and transmission loss (4.5980 dB) occurred at points near the end of rays. The error in travel time standard deviation was negligible throughout the grid.

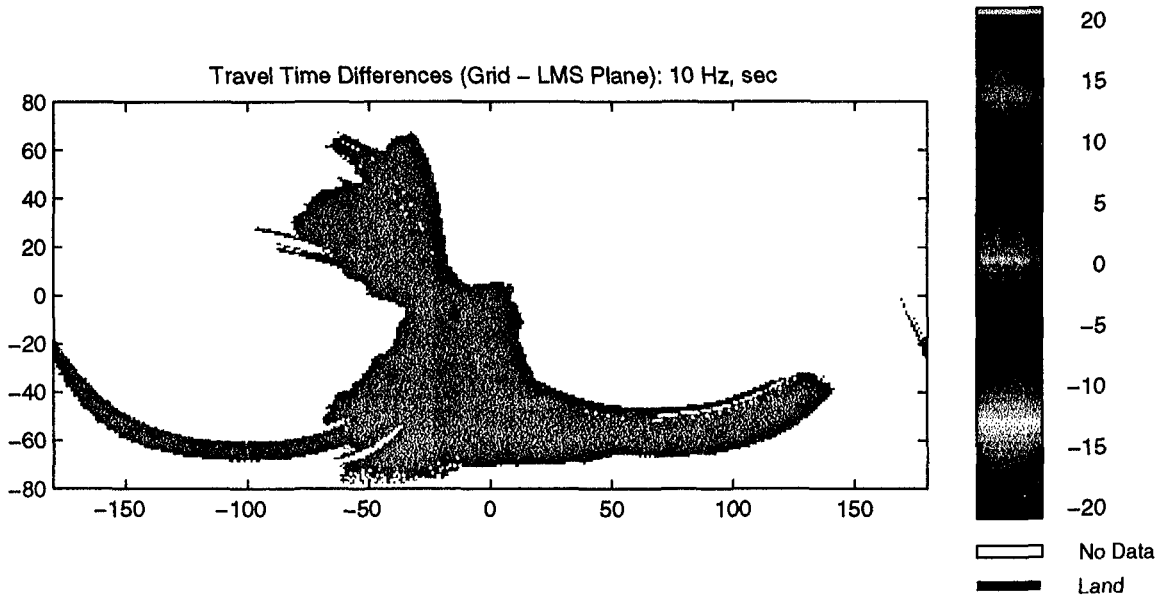

Figure 34: Travel Time Differences (Grid - LMS Plane Interpolated) at 10 Hz

Special processing is necessary for two cases: locations where there is an over-abundance of points (such as in the near field close to the receiver or in high resolution areas) and places where the points are sparse (such as in the far field near the end of rays). In these situations, it is difficult to perform a least mean squares estimate to a plane due to either too many or not enough points. In the former case, only the points which are closest to the center of the cell are used to obtain the least squares estimate; in the latter, several points are artificially added to the cell prior to the interpolation process.

Table 5: Errors (Grid-Interpolated Path) in Geodesic Paths

	$\mu(\lvert E\rvert)$	$\sigma(\lvert E\rvert)$	$Max(\lvert E\rvert)$	$\mu(\lvert E^2\rvert)$	Units
TT	0.1103	0.2138	6.1719	0.0579	sec.
TL	0.0220	0.1200	4.5980	0.0149	dB
σ_{TT}	0.0019	0.0056	0.0690	0.0000	sec.

μ = mean, σ = standard deviation

Finally, the path-to-grid interpolation procedure accounts for multipath. Rays within a cell which arrive from different directions may exhibit markedly different travel times and transmission loss. The degree to which these quantities vary within a particular cell is a function of the specific path geometry and depends on the path length and whether or not the paths interacted with islands or other land masses. An example of the complexity of the ray path structure is shown in Figure 35. Here, refracted rays spaced 0.25 degrees in azimuth were generated from Diego Garcia. In the 12 degree by 20 degree region between South America and Antarctica shown in this figure, note the differences in direction in the rays. Some rays have been refracted around the high resolution region around South Georgia Island (as indicated by the solid lines), others have been refracted north from Antarctica, and still others have not interacted with any islands or land masses. If a cell contains multipath rays, certain assumptions need to be made concerning which path(s) are chosen as input to the interpolation scheme described above in order to obtain a reasonable estimate of the propagation parameters. A primary concern is to choose the paths which are the strongest (least attenuation) and/or arrive first (least travel time).

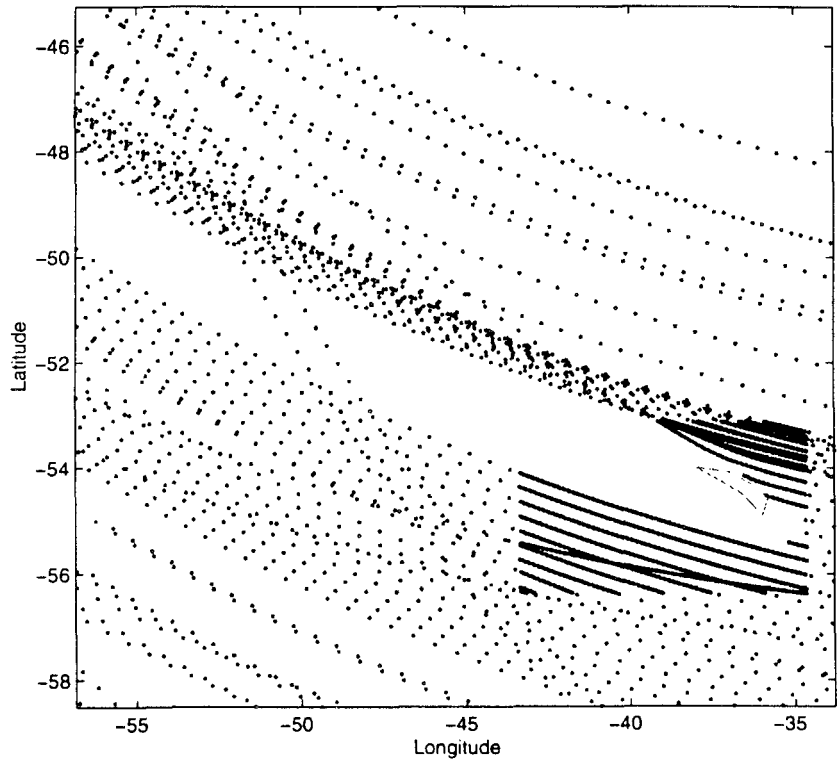

Figure 35: Raypath Structure from Diego Garcia Receiving Station

Using a test case with refracted paths generated from Ascension Island at 10 Hz, several cells which contained rays arriving from different directions were chosen to examine the multipath structure in detail. Based on the analysis, the following approach was derived to detect the presence of multipath within a cell, and to determine which paths should be used as input to the interpolation procedure:

1) Sort rays in a given cell by launch angle from the receiver station.

2) Separate rays into groups (successive rays having launch angles that differ by more than 1° belong to different groups).

3) Sort groups of rays by (average) TL.

4) Retain only those groups of rays for the strongest arrivals (groups having 1 dB more of transmission loss than the previous group are eliminated from the interpolation process).

The final path-to-grid interpolation procedure is summarized in Figure 36, resulting in the eight grids as previously summarized in Table 1. To validate the interpolation algorithm, the values for travel time, transmission loss, and travel time standard deviation for several of these cells were generated using the interpolation procedure and then compared to the levels obtained using the Bisection Method (described in the *HydroCAM Users Guide [3]*) which finds the refracted eigenrays between two points. The results are shown below in Table 6. Several cells without multipath were also analyzed for comparison. The agreement between the two methods was very good for each of the quantities.

Table 6: Comparison of Interpolation and Bisection for Refracted Paths

Interpolated Values

Cell*	TL (dB)	TT (sec)	σ_{TT} (sec)
1	114.052796	3436.459350	0.664724
2	114.091801	3443.542767	0.639052
3	125.344160	5260.961851	2.232267
4	159.637863	11608.928342	5.358468

Differences (Δ = |Interpolation - Bisection|)

Cell*	ΔTL (dB)	ΔTT (sec)	$\Delta\sigma_{TT}$ (sec)
1	0.047204	0.015935	0.035276
2	0.008199	0.157233	0.039052
3	0.044160	0.538149	0.067733
4	0.037863	0.128340	0.041532

*Cell 1. 16 paths, 2 groups of paths (multipath), 13 points in the 'proper' group of paths used for interpolation
Cell 2: 7 paths, 1 group (no multipath), 13 points.
Cell 3 5 paths, 2 groups, 6 points.
Cell 4: 3 paths, 1 group, 5 points.

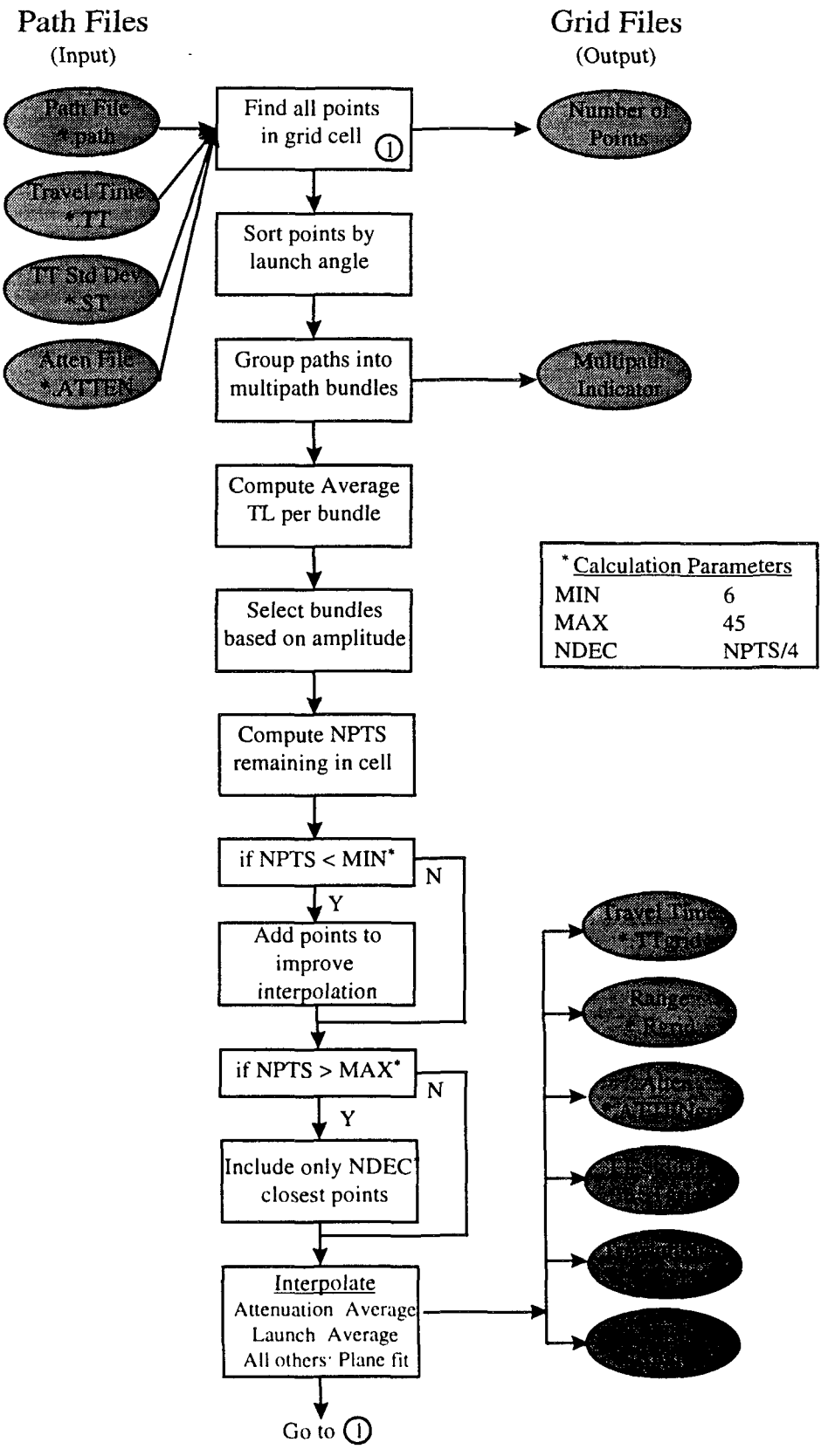

Figure 36: Path-To-Grid Interpolation Process

2.4.3 Stations

Table 7 contains the locations of the IMS stations. These locations were derived from either the latest working papers from the Conference on Disarmament [14] or the Web site of the Prototype International Data Center [15]. Appendix B contains example grid plots for the IMS stations for one frequency and one season. Table D-1 in Classified Appendix D supplies the locations for the NMS stations and contains example grid plots for the NMS stations. A procedure for using HydroCAM to generate grids for new station locations is provided in Appendix A.

Table 7: IMS Station Locations

Station	Latitude	Longitude
Wake Island	19.410	165.856
Ascension 19	-7.8247	-14.6019
Ascension 21	-7.9869	-14.4950
Ascension 26	-8.9442	-14.6178
Ascension 27	-7.8528	-14.3658
Ascension 29	-7.9489	-14.2664
Cape Leeuwin	-35.0	114.2
BOIT/Chagos 1	-6.3	71.0
BOIT/Chagos 2	-7.6	72.5
Crozet 1	-46.3	52.2
Crozet 2	-46.7	51.7
Juan Fernandez 1	-33.3	-78.8
Juan Fernandez 2	-33.9	-78.8
Flores Island	39.3	-31.3
Guadeloupe	16.3	-61.1
Queen Charlotte	52.1	-131.5
Clarion	18.2	-114.6
Tristan	-37.2	-12.5

3.0 Knowledge database validation

A major difficulty with model validation is the lack of quality long-range data sets available for comparison with model predictions. Source and receiver locations, origin time and time of arrival must be known with sufficient accuracy to allow for meaningful travel time comparisons. In addition, both the source and receiver need to be calibrated to accurately measure transmission loss. Signal saturation also makes transmission loss measurements difficult. Inaccurate or incomplete knowledge of these parameters precludes the use of many existing data sets for validation purposes. Several data sets which had sufficient parameters for travel time comparisons were analyzed during last years effort [1] and the results are repeated here for convenience. In addition, data from one other experiment has been analyzed.

Comparisons between predicted and measured travel times and transmission have been made for four data sets. These include measurements from the Heard Island Feasibility Test in January 1991 [16,17], an experiment in March 1960 which used an explosive source off the coast of Australia that was received in Bermuda [18], measurements from the French underground nuclear test at Mururoa Atoll in September 1995 which were received at Pt Sur, California, and measurements made from an underwater weapon effects test (Swordfish) in the Pacific Ocean off the southwestern US in May 1962 [19]. Table 8 summarizes the comparisons that were made using these measurements and predictions from HydroCAM. Unless otherwise indicated, all HydroCAM predictions included the effects of horizontal refraction.

In each experiment, there were varying degrees of uncertainty in the source/receiver locations, the source transmission time and the time of arrival at the receiver. Blank entries in Table 1 for differences in travel time or transmission loss for a particular test indicate that either measured data was unavailable for that quantity or the data was of questionable quality.

All of the transmission loss predictions made by HydroCAM in this analysis assumed the following model:

$$TL(r) = 60 + 10\log_{10}(r) + .00333r + I(r) \qquad (5)$$

where $I(r)$ denotes integrated modal attenuation due to bottom loss and ice cover. Other organizations have used different transmission loss models. The rather large differences in predicted and measured transmission loss shown in Table 8 for nearly all of the cases where reasonable data could be obtained indicates the need for examining this transmission loss model in more detail.

Table 8: Differences Between Predicted and Measured Travel Times and Transmission Losses

Test Source (S),Receivers	Lat / Lon (Deg.)	Path Length (km)	Δ TT [1] (sec)	Δ TL [1] (dB)
1 Heard Island Feasibility Test				
Heard Island (S)	53.4 S / 74.50 E			
Ascension Island	8.07 S / 14.42 W	9220	0.2	8.0
Nova Scotia	38.00 N / 68.00 W	17412		31.0
Christmas (Crab) Island	10.73 S / 105.97 E	5510	-3.7	-8.5 [2] 0.6 [3]
Sri Lanka	3.00 N / 82.00 E	6313		-11.1
Tasman Sea	33.73 S / 162.13 E	6917		1.3
2 Perth to Bermuda				
Perth, Australia (S)	33.22 S / 113.72 E			
Bermuda	32.17 N / 64.58 W	19820.7	4.2	
3 Mururoa to Pt Sur				
Mururoa Atoll (S)	21.83 S / 138.8 W			
Pt Sur, California	36.30 N / 122.39 W	6661.4 [4]	-1.1	
4 Swordfish				
Source	31.25 N / 124.21 W			
Receiver 1	23.63 N / 154.55 W	3100	19.3	
Receiver 2	28.15 N / 122.75 W	366.9	-3.6	

[1] Δ = Predicted - Measured
[2] January 30, 1991
[3] January 31, 1991
[4] Geodesic Path computed by HydroCAM

The measurements for the Heard Island Feasibility Test used a 57 Hz CW transmission. HydroCAM predictions were made using the worldwide and high resolution grids for winter at 50 Hz for phase speed, group speed and attenuation. The SOFAR annual data was used for the group variance and the SOFAR winter data used for the sound channel. ETOPO5 was used for the bathymetry. The travel time prediction at Ascension Island is in excellent agreement with the measurement, only off by 0.2 seconds. The prediction for Christmas (Crab) Island is 3.7 seconds less than the measured value.

For the Perth to Bermuda test, measurements were made from the Australian ship HMAS Diamantina off the coast of Australia using 300 lb. explosive charges. HydroCAM predictions were made at 10 Hz for mode 1 using worldwide grids and high resolution grids near Kerguelen and Crozet Islands, the eastern coast of Brazil and the southern coast of Africa. The ETOPO5 bathymetry database and the annual average sound speed

profiles were used. The travel time prediction exceeds the measurement by 4.2 seconds, which is good considering that the path is nearly antipodal.

Measurements were made from a single hydrophone off Pt Sur California for the French test. The waveform data and receiver coordinates were obtained from the IDC web page. HydroCAM predictions were made for the month of September. Although horizontal refraction was not used for the HydroCAM prediction, clearly from the results in Table 1, the geodesic model predicted travel time is in good agreement with the measured value (1.1 second difference), given the uncertainty in the source coordinates and arrival time.

For the Swordfish experiment, predictions were made using the worldwide and high resolution grids for summer at 50 Hz for phase speed, group speed and attenuation. The SOFAR annual data was used for the group variance and SOFAR data for May used for the sound channel. ETOPO5 was used for the bathymetry. Given that the sound propagated through relatively short distances and benign paths at mid latitudes, the large discrepancies in travel time (19.3 and 3.6 seconds) may be due to inexact time measurements taken at the receivers.

A number of other data sets exist which may be potentially useful for comparison with HydroCAM are listed in Table 9. However, several of the data sets have known limitations inherent to them. These limitations include inexact origin time and location for the source, inaccurate source calibration, and signal saturation at the receiver, which may preclude using the data set for model validation. Sufficient information is currently unavailable as to whether or not data from some of the other sets is of good enough quality to be used for model validation. For these reasons, none of these data sets were analyzed at this time. For some of the tests, information has been provided in Table 9 concerning what data which may be appropriate for comparison (travel time, travel time standard deviation, amplitude, waveform) along with the type of source signal used.

The Chase experiments were a series of events where ships carrying deteriorated explosives were scuttled in deep water [20]. In this type of event, additional complications to the source signal occur due to either pressure induce hull compressions or impact when the hull hits the ocean floor. Unlike events from standard charges (such as SUS), these variations on the source signal require that source measurements be available for appropriate travel time, amplitude or waveform model comparisons.

Project Neptune was an experiment to determine characteristics of long range propagation by dropping specially designed signals at regular intervals along the legs of a US Air Force flight between Bermuda and Perth, Australia. The signals were set to explode in the SOFAR channel and were received at a listening post established off the southern tip of New Zealand [21].

Table 9: Other Potential Data Sets to be Used for Comparison

Name	Dates	Type	Validation*	Limitations**	Availability
Chase21	1970	Chem Expl	W	O,C	Data
Neptune	1964	Chem Expl	T,A	O,L	Paper
Other Chase Series	?	Chem Expl			
Wigwam	1955	Nuclear			
ATOC	1995,1997	Coherent	T,A,ST		Data
French Tests	1970's	Nuclear		O,C	Data
Aleutians	?	Chemical			
Hardtack	1958	Nuclear			

* W = Waveform, T = Travel Time, A = Amplitude, ST = Travel time standard deviation
** O = Origin Time, L = Source location, C = Calibration

Projects Wigwam [22,23,24] and Hardtack [25,26], along with Project Swordfish, may have recorded hydroacoustic signals and other environmental measurements. However, the availability and quality of the data is uncertain at this point.

In summary, high quality data sets for validating long-range acoustic propagation models are extremely limited. Most of the available data is in the form of old reports (1950-1970's), where the control over source location, detonation time and receive time synchronization is questionable. In addition, many of these experiments had overloaded receive electronics, with the additional complication that much of the receiver calibration data has been lost. Our recommendation is that new sources of opportunity (such as seismic exploration, Navy experiments, ship shock trials, etc) be investigated to allow high quality data sets for validation to be obtained. These data should include digital recordings of all available hydroacoustic and seismic sensors, local environmental conditions (sea state and CTD), and if possible, a local calibrated source pressure time series.

4.0 Feasibility of developing a signal envelope database

In addition to travel time and path attenuation grids described previously in this report, it is desired to develop a database of hydroacoustic waveform envelopes for explosive sources. Such a database has several possible functions including:

1) Use as reference signals in automatic detection algorithms
2) Use in analyst displays that allow operators to compare predicted waveforms with measured waveforms from a particular event
3) Correction of mode 1 predicted travel times for "picking" of other modes to account for waveform dispersion and source effects (i.e. corrections for when the arrival times are measured for modes other than mode 1)
4) Use as reference signals for discrimination algorithms, such as templates for comparing the waveform received at long-range versus predictions for several source types and locations (e.g. coastal vented shot versus low-atmosphere shot versus SOFAR fully contained shot measured at the same receiving station)
5) Use of the predicted dispersion to estimate source location from a single sensor.

This section examines the technical issues associated with predicting waveform envelopes in order to assess the feasibility of developing such a database. In Section 4.1, the general modeling issues are discussed. In Section 4.2, an approach is developed for efficiently predicting the envelope of a signal over a limited frequency band. In Section 4.3, an approach for including known oceanographic variability into the envelope model is presented. Section 4.4 concludes with a recommended approach for fully developing this capability.

4.1 Envelope Prediction Issues

Several questions naturally arise when examining the feasibility of predicting waveform envelopes received at long-ranges:

1) Can we construct a model that includes the necessary physics, such as mode coupling and source interactions?
2) Can we compute the envelopes in an efficient manner?
3) Can we include the appropriate environmental uncertainty; both large scale fluctuations and internal-wave scale fluctuations?

Several studies were performed this year address these issues. Previous experience and published results [27] have indicated that fully coherent approaches suffer from too much computation and are too sensitive to specific environmental conditions. Thus, a narrowband approximation to waveform *envelopes* was developed. A methodology to account for the uncertainty accumulated along a travel path due to sound channel fluctuations was also derived. These concepts are summarized in the next two sections.

4.2 Modeling Approach

The goal is to estimate the arrival structure of hydroacoustic signals propagated at long distances across oceans. To this end, a narrowband approximation of the envelope of the signals for the individual normal modes was developed. This approach, consistent with the normal mode basis used for previous investigations, is suitable for use at low frequency and is an application of complex envelope theory used for narrowband signals in the radiowave community. The approximation technique uses a frequency integral over a finite bandwidth, summed over a truncated spectrum of normal modes, to obtain an approximate time series. Modal eigenvalues are then expanded to second order about the center frequency of the band to permit a closed form expression for the time series. The following paragraphs outline this approach. Further details are provided in [28].

In a range independent waveguide, the pressure time series received by a listener at range r and depth z may be approximated as a frequency integral about a center frequency ω_0 over a bandwidth of $2\Delta\omega$ summed over a truncated spectrum of N normal modes with eigenvalues k_n and mode shape functions ϕ_n

$$p(t,r,z) \cong \mathrm{Re}\left\{ \int_{\omega_0-\Delta\omega}^{\omega_0+\Delta\omega} \left(\sum_{n=1}^{N} A(\omega)\phi_n(\omega,z)e^{-i(\omega t - k_n r)} \right) d\omega \right\} \tag{6}$$

Expanding the modal eigenvalues to second order about the center frequency ω_0 and evaluating the amplitude A and the modal eigenfunctions ϕ_n at the center frequency yields the following closed form representation of the complex envelope of a narrowband signal with arbitrary dispersion

$$p(t,r,z) \cong \mathrm{Re}\left\{ \sum_{n=1}^{N} \frac{A(\omega_0)\phi_n(\omega_0,z)e^{-i(\omega_0 t - k_n^0 r)} e^{-i\left(\frac{\left(r\frac{\partial k_n}{\partial\omega} - t\right)^2}{2r\frac{\partial^2 k_n}{\partial\omega^2}}\right)}}{\sqrt{\frac{L}{\pi}\frac{\partial^2 k_n}{\partial\omega^2}}} F \right\} \tag{7}$$

where

$$F = C(\omega_u) + iS(\omega_u) + C(-\omega_l) + iS(-\omega_l) \ , \tag{8}$$

$$\omega_u = \sqrt{\frac{1}{\pi}\frac{\partial^2 k_n}{\partial \omega^2} r}\left(\Delta\omega + \frac{\left(r\frac{\partial k_n}{\partial \omega} - t\right)}{r\frac{\partial^2 k_n}{\partial \omega^2}}\right), \quad \omega_l = \sqrt{\frac{1}{\pi}\frac{\partial^2 k_n}{\partial \omega^2} r}\left(-\Delta\omega + \frac{\left(r\frac{\partial k_n}{\partial \omega} - t\right)}{r\frac{\partial^2 k_n}{\partial \omega^2}}\right) \tag{9}$$

and $C(z)$ and $S(z)$ denote the Fresnel integrals defined by

$$C(z) = \int_0^z \cos(\tfrac{\pi}{2}t^2)dt, \quad S(z) = \int_0^z \sin(\tfrac{\pi}{2}t^2)dt \ . \tag{10}$$

Since closed form approximations for the Fresnel integrals are available in standard numerical methods texts, the approximate waveform computed using (7-10) should be much faster than the direct numerical integration required by the coherent synthesis of equation (6). The performance of this narrowband approximation was investigated for several waveguides of interest. The sound speed profile used is illustrated in Figure 37. For deep water it corresponds to a SOFAR channel type profile. If it is truncated at a shallow depth it has the downward refracting properties typical of many shallow water areas. For water depths of 250 and 5000 meters, Kraken was run at 0.1 Hz increments from 10 Hz to 80 Hz to determine the complex wave numbers corresponding to the normal modes. The deep water waveguide supports approximately $2f$ modes, where f is the frequency in Hz, with a mode 1 cut-off frequency of approximately 0.15 Hz, while the shallow water waveguide supports far fewer modes, with the cut-off of the first mode occurring at approximately 6 Hz and only seven modes being supported at 100 Hz.

In addition to the phase and group speeds, the second partial derivative of the modal wavenumber with respect to frequency is required. If this dispersion term is positive, then higher frequencies travel slower than low frequencies, while the opposite is true if this second derivative is negative.

In Figure 38, comparisons are shown between a narrowband (coherent) synthetic of the arrival structure summed across all modes and the complex envelope prediction in the SOFAR channel (5000m depth) at a range of 10,000 km at 10 Hz for bandwidths of 1, 2, and 3 Hz. The modal slowness required for the complex envelope prediction was determined at the center frequency by a depth integral of the mode shape functions. The dispersion term ($\frac{\partial^2 k_n}{\partial \omega^2}$) was computed by finite differences. Consistent with an incoherent mode model, the sum of the modal envelopes was performed in power space, and the square root of the result taken to obtain a time series envelope $\bar{p}(t)$.

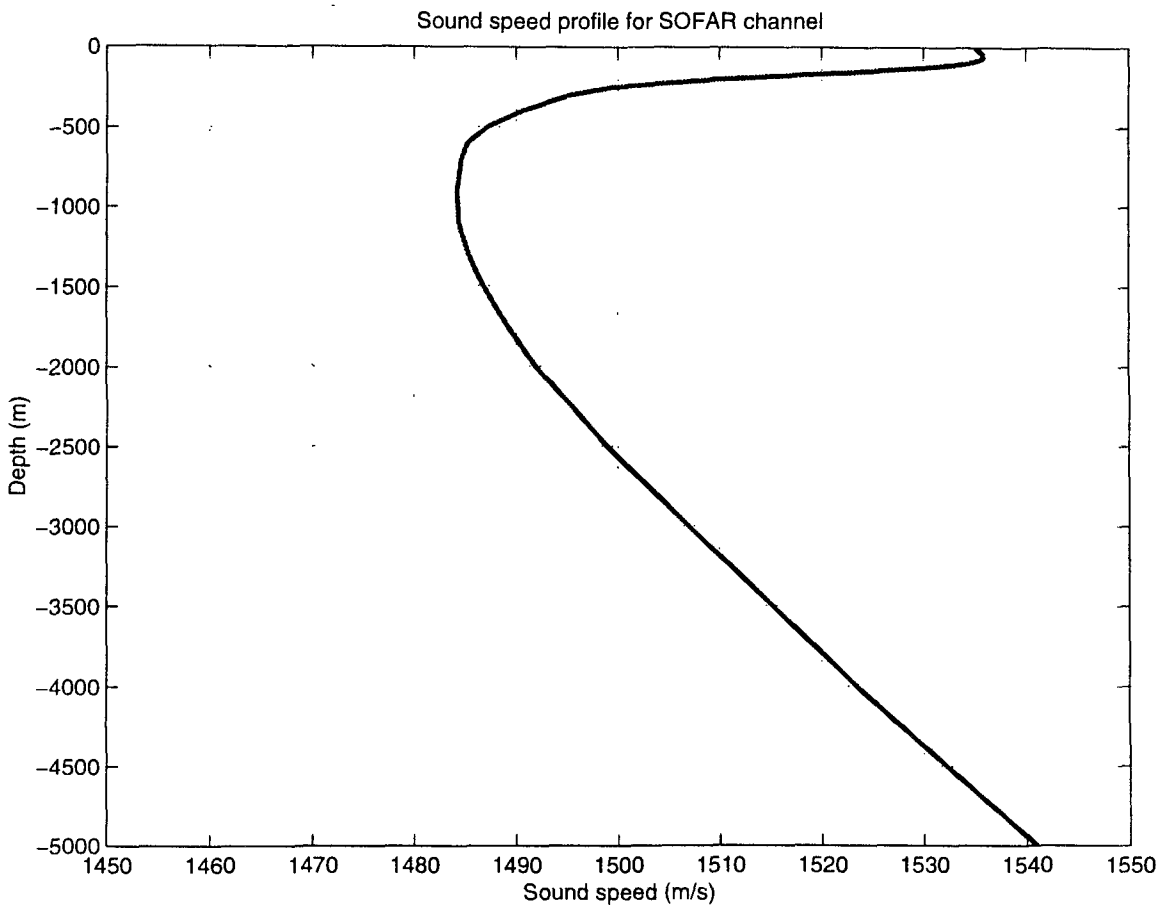

Figure 37: Sound Speed Profile used in Waveform Analysis

In Figure 38, the synthetic (coherent) envelopes are shown in gray, and the narrowband approximations are shown in black for the first 10 modes. For the mode number indicated by -1, the synthetic time series shown in gray is summed across all modes with the complex envelope approximation $\pm\underline{p}(t)$ superimposed in black. As expected the narrowband approximation does better for narrower frequency bands. The approximation also appears to work better for the lower mode numbers. However, the overall form of the arrival envelope, summed across all modes, is generally predicted quite well. Note that the bandwidths over which the complex envelopes are predicted correspond to one-sided bandwidths of $f/10$, $f/5$ and $3f/10$, and that the $f/10$ bandwidth gives the best result.

Similar results for the shallow water waveguide (250m depth) are illustrated in Figure 39 at a range of 100 km at 10 Hz for the same bandwidths. In general, the results for shallow water are as good or better than the corresponding deep water results, due to the better behavior of the approximation for low mode numbers, and the corresponding lower number of supported modes. Further details are provided in [29].

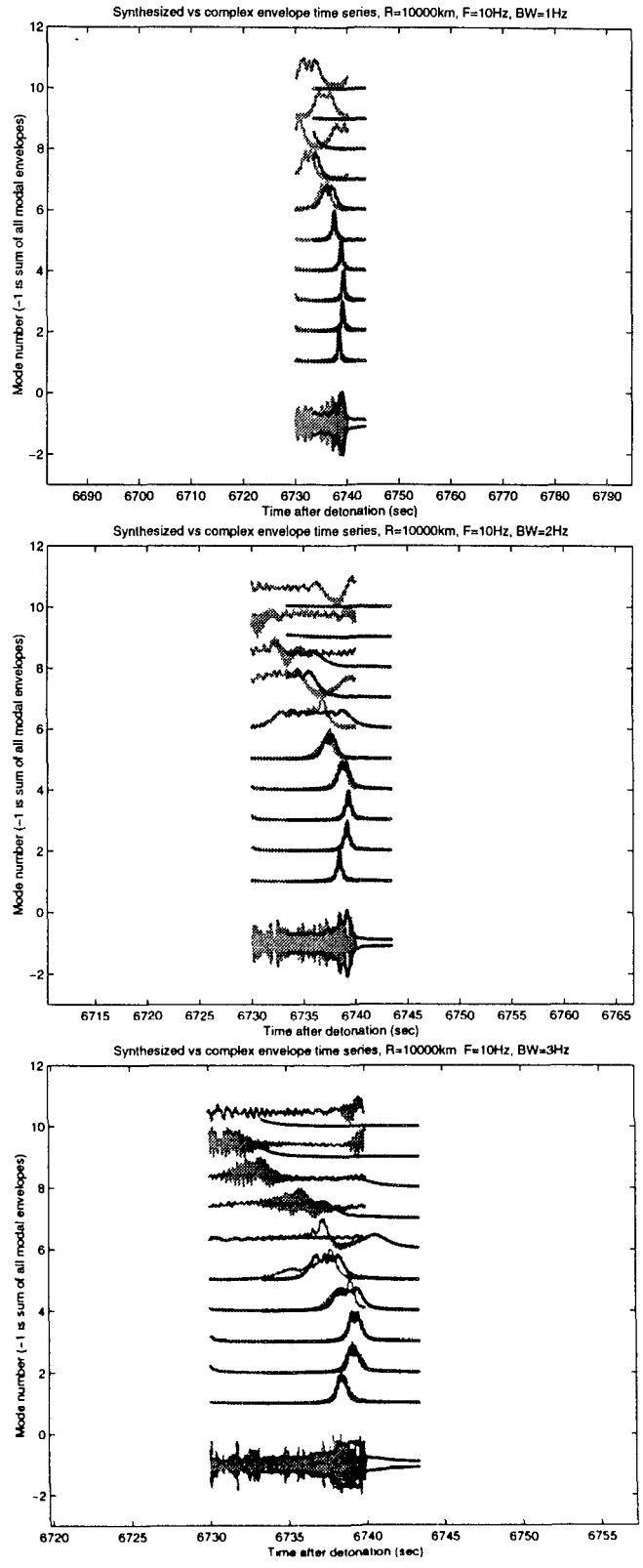

Figure 38: Approximate Arrival Envelope vs Coherent Synthetic for a SOFAR Channel

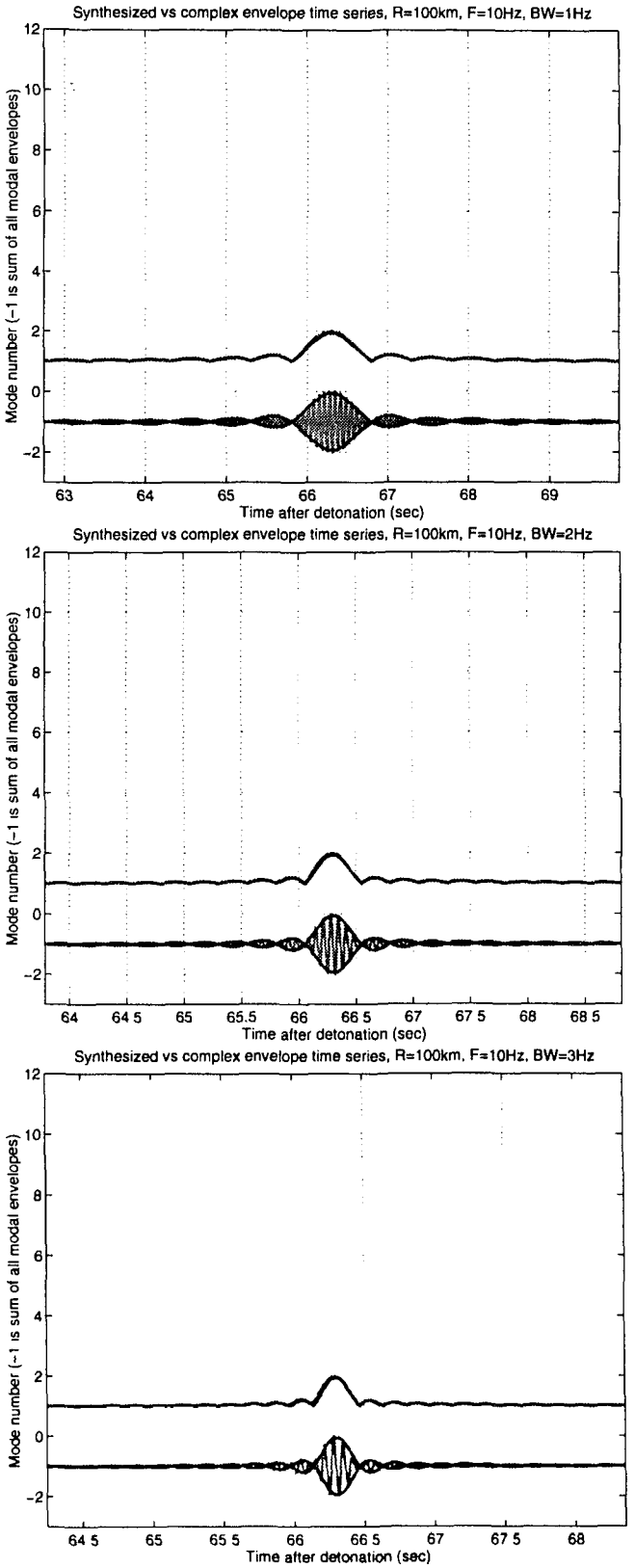

Figure 39 Comparison of Approximate Arrival Envelope to Coherent Synthetic for a Shallow Water Waveguide

4.3 Accounting for oceanographic variability

As acoustic waves travel through the ocean, they encounter local variations in the sound speed structure which fall into two general categories:

1) biases between annual or seasonal average sound speeds contained in historical databases and specific realizations averaged over the same length scales (typically 1 degree resolution)

2) fine scale structure which is inadequately accounted for in the databases, such as internal wave activity.

Because of these sound speed uncertainties, predicted waveforms which coherently superimpose modes across the frequency band of interest to synthesize a snapshot of a particular realization of the sound field may vary significantly from an actual measured arrival time series. The degree of fluctuation in a predicted time series is compounded due to the global nature of the propagation problem being considered. It is therefore useful to estimate the expected arrival structure of a time series averaged over a large number of realizations of sound channel variability.

A model is proposed for a time series received at a large distance from a source which is parameterized not only by deterministic variables such as center frequency, bandwidth, and source and receiver depth, but also on the uncertainty accumulated along the path due to sound channel fluctuations [30]. If it assumed that perturbations in the sound channel introduce local fluctuations in the wavenumber and modal group speed, and that these fluctuations are not significant to cause mode coupling, then the time series received at long range from a source is given by

$$p(t,r,z) \cong \mathrm{Re}\left\{ \sqrt{2\pi} \sum_{n=1}^{N} \frac{e^{-i\left(\omega_0 t - \int_0^r (k_n^0(r') - \Delta k_n(r'))dr'\right)}}{\sqrt{\int_0^r k_n^0(r')dr'}} \phi_n(\omega_0, z_s)\phi_n(\omega_0, z) \right.$$

$$\left. \times \int_{-\Delta\omega}^{\Delta\omega} e^{-i\omega\left(t - \int_0^r (S_n(r') - \Delta S_n(r'))dr'\right)} d\omega \right\} \qquad (11)$$

where z_s represents source depth, $S_n = \frac{\partial k_n}{\partial \omega}$ is modal slowness and $\Delta k_n(r')$, $\Delta S_n(r')$ are the deviations in the modal wavenumbers and slowness due to perturbations in the local sound speed structure at r'.

In order to examine the intermodal correlation of wavenumber and slowness deviations due to sound speed perturbations, the sound speed fluctuations are decomposed into empirically orthogonal functions (EOFs). These functions are, by definition, uncorrelated for the particular data from which they were obtained, but are also assumed to be statistically independent [31]. It is useful to understand how the decorrelation between adjacent modes dictates the expected behavior of a received time series. These decorrelations are caused by the differences in responses of the individual modes to the common sound speed perturbations encountered as they travel along the propagation path. The use of EOFs allows these differences to be decomposed into uncorrelated components. If only one EOF is used then the perturbations between all the modes remain entirely correlated.

By expanding the sound speed perturbations in terms of the EOF and their range dependent coefficients, the range integral of the deviations to the modal wavenumber and slowness can be determined in terms of known constants and the range integral of the EOF coefficients. The range integrals of the EOF coefficients themselves are assumed to be zero mean Gaussian random variables. A short time average of the square of the time series given by equation (11) and its expected value is then calculated from these quantities. The decorrelation between adjacent modes for a specific time can then be evaluated using the standard deviation of the range dependent coefficients. The intermodal decorrelation terms computed are identical to those in [31] and are associated only with the center frequency of the calculation and the statistics of the sound channel fluctuations. Further details of this approach are given in [32].

4.4 Recommendations for development of the database

Based on the initial findings as discussed in the previous paragraphs, the prognosis appears to be good for developing a computationally efficient technique for generating waveform grids. Future efforts to further develop the database include:

1) Develop the software for the waveform envelope model (including the environmental variability calculations) in C++.
2) Integrate range dependent environmental characteristics into the model
3) Integrate source characteristics from CALE/NPE into the model
4) Validate against any available waveform measurements
5) Update HydroCAM documentation to include the physics and use of the model
6) Perform sensitivity studies to determine appropriate grid resolution, including the time/frequency and spatial sampling needed for accurate predictions, the sensitivity of waveform prediction methodology to the environmental variability, and the effects of specific sources and scenarios

5.0 Conclusions and recommendations

HydroCAM has been used to generate propagation characteristic grids which can be used as components of the hydroacoustic knowledge database required by operational monitoring systems. These grids include travel time, travel time standard deviation, range, and attenuation correction as predicted from a given station to all source locations on the grid. Other grids, including multipath, launch angle and transmission loss have also been generated and can be used as input to network performance algorithms and to assist in the interpretation of the travel time and attenuation grids.

In addition, modal property grids, including phase speed, group speed, modal attenuation and modal slowness variance, have also been generated as an intermediate step in producing the propagation grids. All grids have been generated for winter, spring, summer and fall to account for seasonal fluctuations in the sound velocity profiles, and for two frequencies: 10 Hz and 50 Hz. The grids include propagation effects due to horizontal refraction and are generated for mode 1 only.

5.1 Databases and parameters

A number of sensitivity analysis and tradeoff studies were performed to determine the appropriate databases and parameters to be used as input to HydroCAM to generate the modal and propagation characteristic grids.

Modal Grids

Fifty-one geographic regions were identified which needed modal characteristics at finer resolution than the nominal 1° worldwide grid resolution. These areas included regions near islands or coastlines where ray paths originating from monitoring stations were likely to interact with bathymetric features. Propagation in these regions is dominated by the refraction caused by rapid changes in bathymetry and sound velocity structure. Five minute resolution was determined to be appropriate for these regions. If new monitoring stations are added to the network, additional high resolution areas may be required.

A WKB model was selected as the acoustic mode model to generate the modal property grids due to its significant savings in execution time given the large number of runs required. Numerous comparisons were made between phase speed, group speed and attenuation generated by WKB with those computed with the Kraken model. The differences were insignificant for the test cases considered. However, if in the future complete sets of modes are required (such as with the waveform envelope model), WKB will lose much of its computational advantage and Kraken should be used.

The differences in phase and group speed using different sound speed databases was significantly more than the differences exhibited by WKB and Kraken. This suggests that the choice of a proper sound speed database (and interpolation of sound speed profiles) weighs more heavily in generating accurate propagation grids than the choice of a mode model. For this effort, WOA was chosen for global calculations and GDEM for high resolution regions.

Path Attenuation

Several equations for the "baseline" attenuation are currently used by different organizations. Each accounts for the injection of energy into the SOFAR channel, cylindrical spreading, and dispersion and volume attenuation in a slightly different way. In addition, the AFTAC model (which most likely has the largest amount of long-range empircal data behind it) is referenced to sources at 35 geographic degrees (vs the standard 1 meter). These model differences have important implications especially if the "range" and "amplitude correction" grids generated under this effort are to be used for estimating the source level for discrimination or source identification. It is recommended that an effort be undertaken to determine the appropriate factor needed to rescale the AFTAC model back to 1 meter; which would allow consistency with other models (such as the pressure-time series generated by the CALE/NPE model) and other archived measurements. Since the SOFAR channel coupling terms in any model will depend greatly on the details of the source and the local ocean environment, a determination of the appropriate baseline analytic model (or simple first-order correction terms) based on the source type and local environment should be undertaken.

Due to the limited amount of unclassified bottom data, a simple fluid halfspace model which assumed constant bottom sound speed, density and attenuation was used to account for bottom loss. Comparisons of phase speed, group speed and attenuation were made between predictions using these parameters and those from a standard Navy database with the results in agreement to within 10%. If, in the future, bottom interactions become increasingly important, this database (or others) could be integrated into HydroCAM. The disadvantage to this is that the grids themselves may then become classified, depending on the specific database used.

Attenuation due to ice cover is now included in the grids, using a first order model and measurements from ONR experiments performed in the central Arctic [13].

It was determined that losses due to rough surface interaction was at least five orders of magnitude less than that for ice cover and bottom at mid-latitudes, and an order of magnitude less at high latitudes, except under extreme conditions which would already include ice coverage. Thus, surface attenuation was not included into the grid generation scheme.

Path-to-Grid Interpolation

A least mean squares approach to interpolate non-uniformly spaced data within a cell was used to approximate the data values at the center of the cell. Overall, the errors induced by this procedure were small when compared with data from a uniformly spaced grid. The errors tend to be concentrated in cells containing a large number of points (such as in the near field close to a receiving station or in high resolution regions) and in cells containing only a few points (far from the receiving station). Procedures have been implemented to reduce these effects, but some bias error may still exist for some cases and other methods may need to be considered to further reduce these errors. As a specific example, if very high accuracy is needed for sources close to a given monitoring station (with several hundred km), then values in the current grids should be replaced with values calculated using eigenrays to those specific cells.

5.2 Travel time biases

An important issue this year was to examine and quantify travel time biases due to frequency, seasonal fluctuations in the sound velocity profile and the type of model used in the raytrace algorithm (geodesic vs. horizontal refraction). Of these parameters, the largest biases exhibited were due to the choice of model.

1) Large regions in the southern oceans showed 20-30 second travel time biases when comparing geodesic paths using sound channel speed with paths generated with horizontal refraction using modal phase and group speeds. A maximum of 60 seconds was observed for near-antipodal paths. This clearly demonstrates the need for a raytrace model with horizontal refraction which uses modal speeds.

2) Travel time biases of up to 25 seconds for high latitude paths were observed when comparing grids generated at 10 Hz and 50 Hz.

3) Seasonal fluctuations exhibited up to 15 second travel time biases for high latitude paths.

5.3 Knowledge database validation

Several data sets which had measured values for travel time and transmission loss were used to compare against HydroCAM predictions. Most of the travel time predictions compared favorably with measured results, while many of the transmission loss predictions had larger errors.

It should be emphasized that high quality data sets for validating long-range acoustic propagation models are extremely limited. Most of the available data is in the form of old reports (1950-1970's), where the control over source location, detonation time and receive time synchronization is questionable. In addition, many of these experiments had overloaded receive electronics, with the additional complication that much of the receiver calibration data has been lost. Our recommendation is that new sources of opportunity (such as seismic exploration, Navy experiments, ship shock trials, etc) be investigated to allow high quality data sets for validation to be obtained. These data should include digital recordings of all available hydroacoustic and seismic sensors, local environmental conditions (sea state and CTD), and if possible, a local calibrated source pressure time series.

5.4 Waveform envelope prediction

A narrowband approximation was developed to efficiently predict waveform envelopes for explosive sources. The technique was based on a frequency integral over a finite bandwidth summed over a truncated spectrum of normal modes to obtain an approximate time series. Comparisons were made to synthetic signals for deep and shallow water, at 10 Hz for several bandwidths with promising results. Future efforts should include range dependent environmental data, include source effects using the CALE/NPE source model and validate the model with actual waveform data.

6.0 References

[1] T.R. Farrell, K.D. LePage, *Development of a Comprehensive Hydroacoustic Coverage Assessment Model,* PL-TR-96-2248, September 1996.

[2] K.D. Heaney, W.A. Kuperman and B.E. McDonald. "Perth-Bermuda Sound Propagation (1960): Adiabatic Mode Interpretation", JASA **90**(5), November 1991, p. 2589.

[3] T.R. Farrell, K.D. LePage, C. Barclay, *Users Guide for the Hydroacoustic Coverage assessment Model (HydroCAM),* BBN Technical memorandum W1273, August 1996.

[4] M.B. Porter, *The Kraken Normal Mode Program,* SACLANT Undersea Research Centre, October 30, 1995.

[5] Levitus and Boyer, "World Ocean Atlas 1994 Volume 4: Temperature", NOAA Atlas NESDIS 4, Washington, DC. June 1994.

[6] *Database Description for the Master Generalized Digital Environmental Model (GDEM) Version 5.0,* OAML DBD-20F, Naval Oceanographic Office, Stennis Space Center MS. September 1995.

[7] L.W. Row III, D.A. Hastings, P.K. Dunbar, *TerrainBase, Worldwide Digital Terrain Data, Documentation Manual,* US Department of Commerce, National Oceanic and Atmospheric Administration. April 1995.

[8] W.H.F. Smith, D.T. Sandwell, "Global Seafloor Topography from Satellite Altimetry and Ship Depth Soundings", recently submitted.

[9] General Bathymetric Chart of the Oceans (5th Edition), International Hydrographic Organization / Intergovernmental Oceanographic Commission / Canadian Hydrographic Service, 1984.

[10] I.A. Fraser and P.D. Morash, "Observation of the Heard Island Signals Near the Gulf Stream", JASA 96(4), 2448-2457, 1994.

[11] E.L. Hamilton, "Acoustic Properties of Sediments", in *Acoustics and the Ocean Bottom*, edited by A. Lara-Saenz, C. Ranz-Guerra, and C. CarboFite (Consejo Superior de Investigaciones Cientificas, Madrid, 1987), pp. 3-58.

[12] A.C. Kibblewhite, "Attenuation of Sound in Marine Sediments: A Review with Emphasis on new Low-Frequency Data", JASA 86, 716-738 (1989).

[13] Duckworth, Farrell, LePage, and Atkinson "Arctic LFA Program Final Report", BBN Technical Report No W1226, ONR/AEAS Technical Report 94-S102, September 30, 1994 (SECRET/NOFORN Report).

[14] *Report of the Expert Group based on Technical Discussions held from 4 through 15 December 1995, Working Group 1 - Verification,* Conference on Disarmament Paper CD/NTB/WP.283, 20 December 1995.

[15] Prototype International Data Center Web Site – http://www.cdidc.org/

[16] JASA **96** (4) , October 1994. This issue contains a collection of papers describing the Heard Island Feasibility Test (HIFT).

[17] D.R. Palmer, T.M. Georges, J.J. Wilson, L.D. Weiner, J.A. Paisley, R. Mathiesen, R.R. Pleshek and R.R. Mabe. "Reception at Ascension of the Heard Island Feasibility Test Transmissions", JASA **96** (4), October 1994.

[18] R.C. Shockley, J. Northrop and P.G. Hansen. *SOFAR Propagation Paths from Australia to Bermuda: Comparison of Signal Speed Algorithms and Experiments,* JASA **71** p. 51, January 1982.

[19] T. McMillian, W.P. de la Houssaye, C.T. Jonhson, "Operation Dominic Shot Swordfish: Effects of an Underwater Nuclear Explosion on Hydroacoustic Systems (U)", US Navy Electronics Laboratory, August 1964, SECRET.

[20] A.C. Kibblewhite and R.N. Denham. "Hydroacoustic Signals from the CHASE V Explosion", JASA **45** (4), October 1969.

[21] A.C. Kibblewhite, R.N. Denham, and P.H. Barker. "Long-Range Sound-Propagation in the Southern Ocean - Project Neptune", JASA **38** (4), October 1965.

[22] C.J. Aronson, et al. "Underwater Free-Field Pressures to Just Beyond Target Location", Project 1.2, Operation Wigwam, WT-1005, May 1957, US Naval Ordnance Laboratory, White Oak, CONFIDENTIAL Formerly Restricted Data.

[23] F.B. Porzel, "Close-in Time of Arrival of Underwater Shock Wave", Project 4.4, Operation Wigwam, WT-1034, May 1957, Armour Research Foundation, Illinois Institute of Technology, CONFIDENTIAL.

[24] T. McMillian, "Underwater Free-Field Pressure Measurements", Project 1.3, Operation Wigwam, WT-1007, June 1956, US Navy Electronics Laboratory, CONFIDENTIAL.

[25] E. Swift Jr., et al, "Underwater Pressures from Underwater Bursts", Project 1.1, Operation Hardtack, WT-1606, August 1960, Waterways Experiment Station and US Naval Ordnance Laboratory, White Oak, CONFIDENTIAL Formerly Restricted Data.

[26] C.J. Burbank et al, "Refraction of Shock from a Deep Water Burst", Project 1.5, Operation Hardtack, WT-1610, October 1960, US Navy Electronics Laboratory, CONFIDENTIAL Formerly Restricted Data.

[27] M.D. Collins and W.A. Kuperman, *Overcoming Ray Chaos*, JASA **95**, p 3167-3170 (1994).

[28] K.D. LePage, *Broadband Envelopes of Modal Arrivals*, BBN Technical Memorandum, April 11, 1997.

[29] K.D. LePage, *Comparison of Broadband Envelopes and Synthesized Modal arrivals for Propagation in Shallow and SOFAR Channels*, BBN Technical memorandum, April 29, 1997

[30] K.D. LePage, *Variability of Arrival Time Series Structure at Global Scales*, BBN Technical Memorandum, August 24, 1997

[31] J.L. Krolik, "Matched Field Minimum Variance Beamforming in a Random Ocean Channel", J. Acoust. Soc. Am., 92 (3) 1408-1419 (1992)

[32] K.D. LePage, *Expressions for Modal Properties Important for the Prediction of Refraction and Arrival Statistics at Global Scales*, BBN Technical memorandum, September 1996.

7.0 Acronyms

AFTAC	Air Force Technical Applications Center
AOU	Area of Uncertainty
ASW	Anti-Submarine Warfare
CTBT	Comprehensive Test Ban Treaty
DOE	Department of Energy
ESL	Energy Source Level
FD	Finite Differences
GDEM	Generalized Digital Environmental Model
HARPO	Hamiltonian Acoustic Raytrace Program for the Ocean
HR	Horizontal Refraction
HydroCAM	Hydroacoustic Coverage Assessment Model
IMS	International Monitoring System
IVSEM	Integrated Verification System Evaluation Model
JASA	Journal of the Acoustical Society of America
LLNL	Lawrence Livermore National Laboratory
NJIT	New Jersey Institute of Technology
NOAA	National Oceanographic and Atmospheric Administration
NMS	National Monitoring System
NPE	Non-linear Parabolic Equation
NRL	Naval Research Laboratory
RAM	Range-dependent Acoustic Model
SNL	Sandia National Laboratory
SNR	Signal to Noise Ratio
SOFAR	Sound Fixing and Ranging
SONAR	Sound Navigation and Ranging
TL	Transmission Loss
USGS	United States Geologic Survey
WHOI	Woods Hole Oceanographic Institution
WKB	Wenzel-Kramers-Brillouin
WOA	World Ocean Atlas

Appendix A: Procedure for using HydroCAM to calculate grids for new station locations

If you are a HydroCAM user, you can generate the propagation grids for new station locations using a simple MATLAB script. Please contact Jeff Angell or Ted Farrell at BBN for additional information.

(1) Make sure that the station location has a valid HydroCAM receiver file, and is included in a HydroCAM network. (See the HydroCAM users manual [3] for how to add a receiver file or a new network).

(2) Go to the directory where the grid files have been dumped from the distribution tape. You should see the following subdirectories:

- matlab
- raytraces
- kb_grids

(3) In the matlab directory, edit the file make_kb_grids.m. This file contains all of the information necessary to generate the grids. Edit the file to use the frequency, season and network that you desire. When you are done, execute "make_kb_grids" from the MATLAB prompt. This function will create a Unix shell script for generating the grids.

(4) At the Unix prompt, execute the script. The global raytrace program (GlobeRay) will compute the ray paths. This program will be followed by PathToGrid, which interpolates the raypaths onto a regular lat/lon grid.

Again, please contact BBN for any additional information that may be required.

Appendix B: Example grid plots for IMS Stations

The following displays show the travel time, attenuation correction, travel time standard deviation and multipath indicator grids for the Summer season at 50 Hz. A single plot is provided for each station in the IMS. The station locations are as indicated in Table 8 of the main body of this report.

Wake Island, 50 Hz, Summer

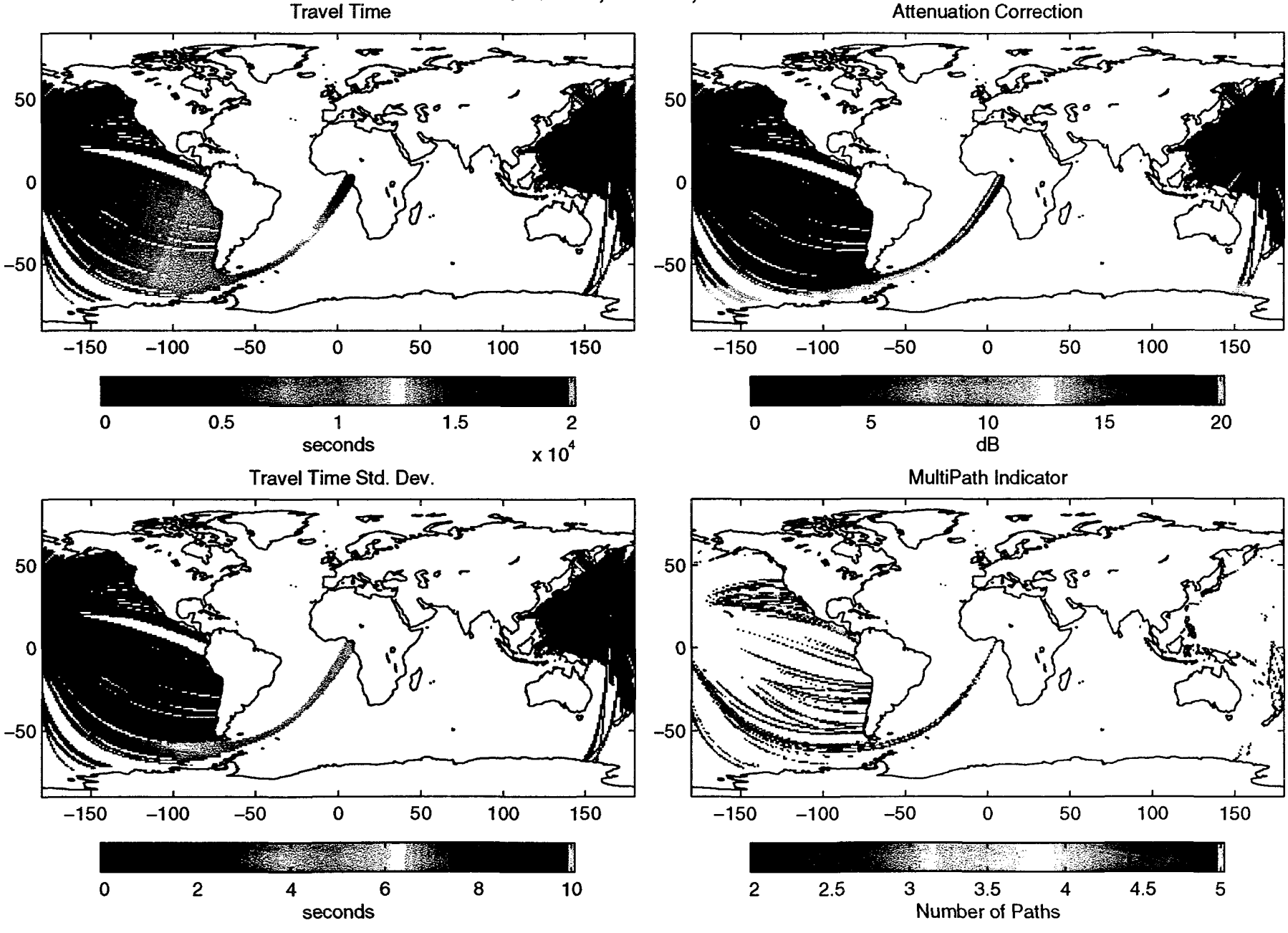

Ascension 19, 50 Hz, Summer

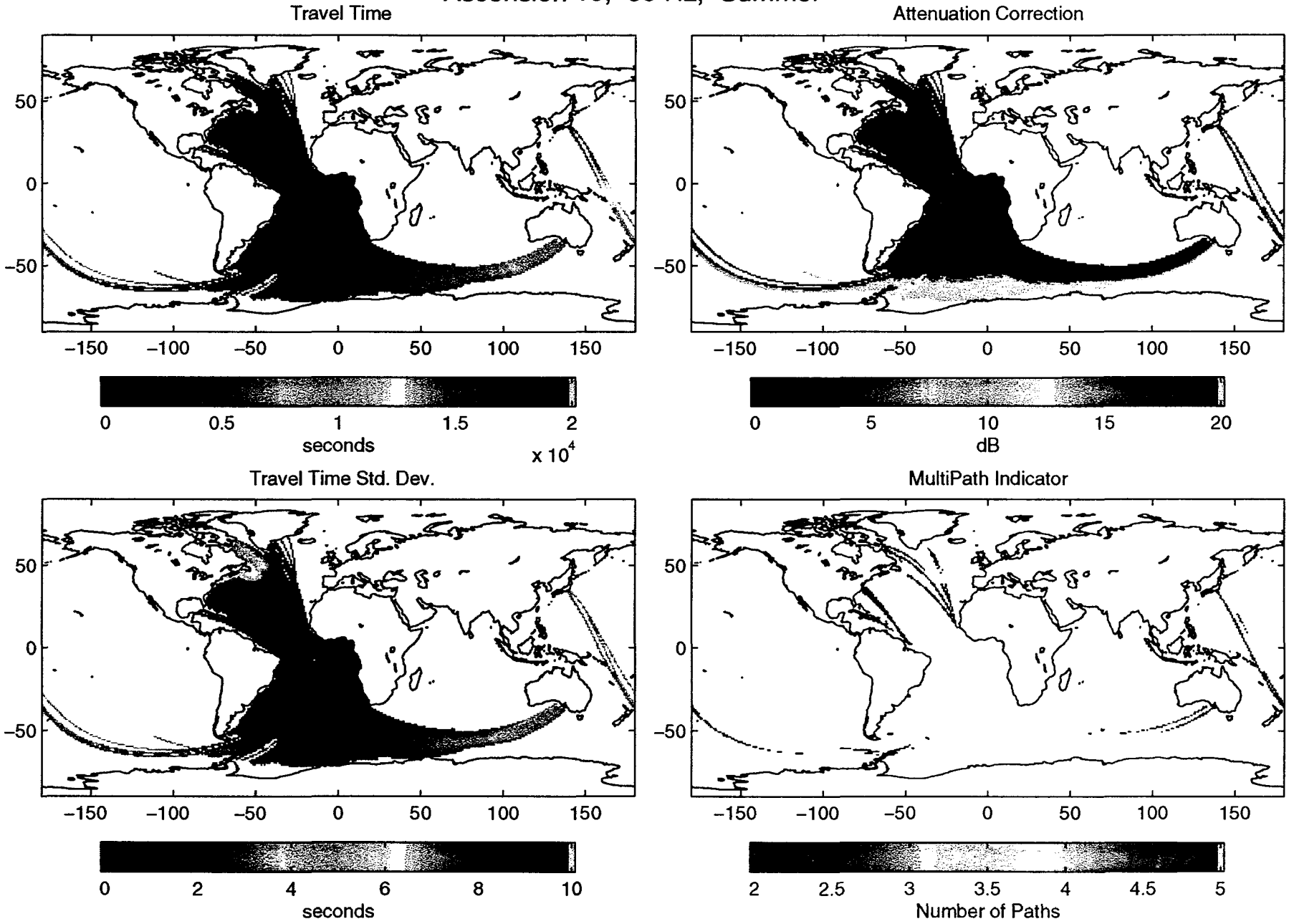

Cape Leeuwin, 50 Hz, Summer

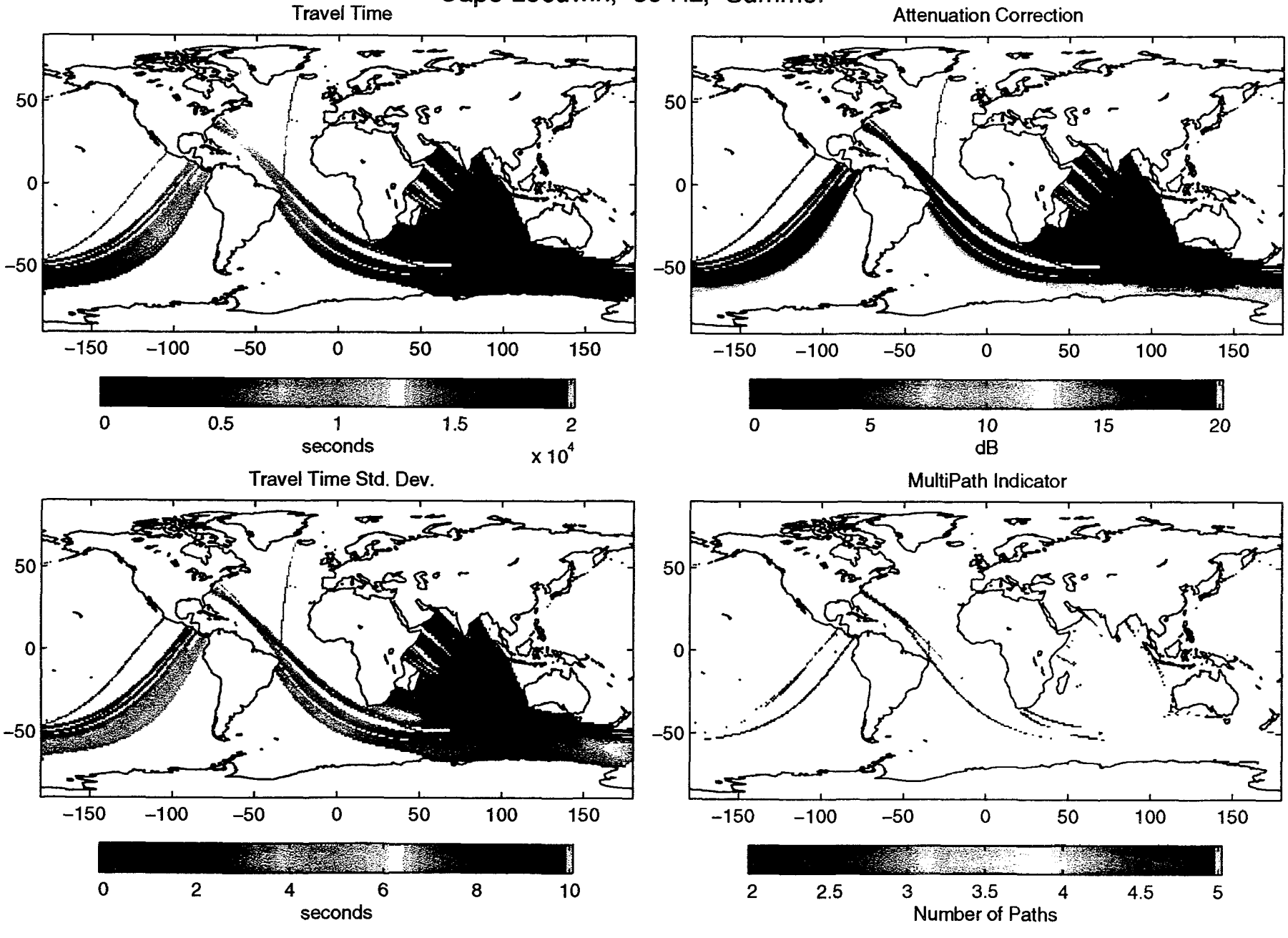

Crozet 1, 50 Hz, Summer

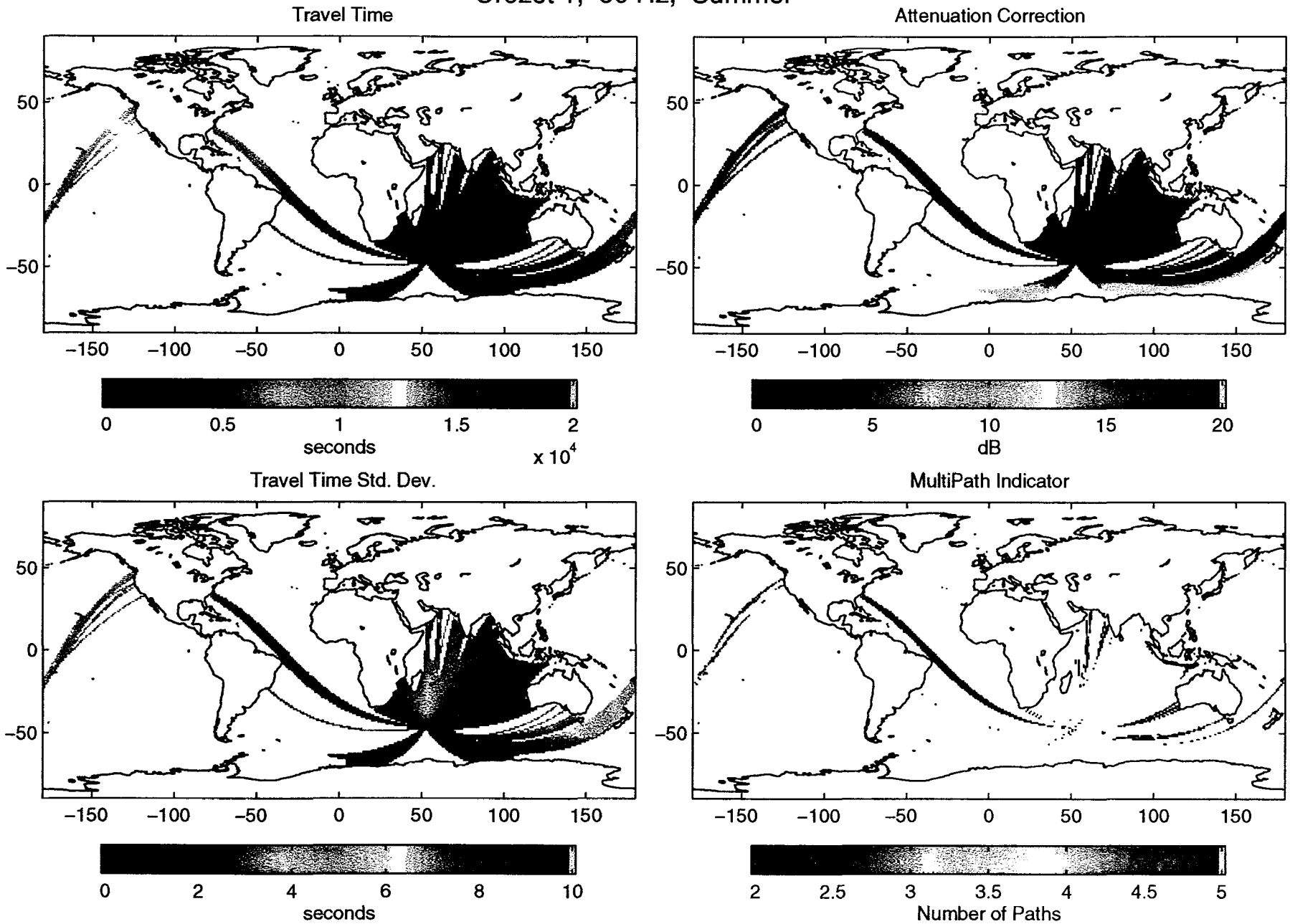

Appendix C: Rough Surface Loss Analysis

The purpose of this appendix is to summarize a study of the expected magnitude of the losses due to interaction of acoustic energy with a rough sea surface at low frequencies. It is shown that only modes which directly interact with the sea surface suffer any appreciable loss due to scattering. Since regions of the earth with surface interacting modes correspond closely to regions covered by ice; and since ice cover attenuation is much larger than rough surface attenuation, it is felt that rough surface attenuation may be neglected in first order attenuation calculations. Additional details on this study are available in reference [C1].

For clarity the attenuation due to rough surface interaction is briefly derived. This development closely follows two papers by Kuperman [C2 and C3]. To second order the perturbed boundary conditions at the rough surface are

$$\underbrace{\phi}_{O(1)} + \underbrace{\eta\frac{\partial\phi}{\partial z} + s}_{O(\varepsilon)} + \underbrace{\eta^2/2\frac{d^2\phi}{\partial z^2} + \eta\frac{\partial s}{\partial z}}_{O(\varepsilon^2)} + O(\varepsilon^3) = 0, \qquad \text{(C-1)}$$

where η, the surface height excursion due to roughness, and s, the scattered field, are both considered small parameters of order ε. The zeroth order equation is simply the homogeneous equation for the unperturbed boundary

$$\phi = 0,$$

while the first order equation for the scattered field is

$$s = -\eta\frac{\partial\phi}{\partial z}. \qquad \text{(C-2)}$$

Insertion of equation (C-2) into equation (C-1) and averaging over zero mean Gaussian random variables η and s yields the self consistent equation for the mean field

$$\left\{1 + \langle\eta^2\rangle/2\frac{\partial^2}{\partial z^2} - \left\langle\eta\frac{\partial}{\partial z}\left(\eta\frac{\partial}{\partial z}\right)\right\rangle\right\}\langle\phi\rangle = 0. \qquad \text{(C-3)}$$

Since we are interested in the field at a horizontal wavenumber k_m corresponding to a mode, we are interested in the transform (with respect to k_m) of equation (C-3)

$$\left\{1 - \langle\eta^2\rangle/2\left(k_0^2 - k_m^2\right) - F.T.\left[\left\langle\eta\frac{\partial}{\partial z}\left(\eta\frac{\partial}{\partial z}\right)\right\rangle\right]\right\}\langle\tilde{\phi}(k_m)\rangle = 0; \qquad \text{(C-4)}$$

The indicated Fourier transform of the last term may be expressed as the double convolution of the individually transformed terms

$$F.T.\left[\left\langle \eta\frac{\partial}{\partial z}\left(\eta\frac{\partial}{\partial z}\right)\right\rangle\langle\phi\rangle\right]=\frac{1}{4\pi^2}\int dq\left\langle\tilde{\eta}(k_m-q)\frac{\partial}{\partial z}\int dk'\tilde{\eta}(q-k')\right\rangle\frac{\partial\langle\tilde{\phi}(k')\rangle}{\partial z}. \quad \text{(C-5)}$$

For uncorrelated wavenumber bins of a homogeneous random process and using the fact that we are analyzing plane waves, equation (C-4) may be explicitly written as an effective mean free surface impedance condition

$$\left\{1-\langle\eta^2\rangle/2\left(k_0^2-k_m^2\right)\right\}\langle\tilde{\phi}(k_m)\rangle=\frac{1}{2\pi}\int dqi\sqrt{k_0^2-q^2}\,P(k_m-q)\frac{\partial\langle\tilde{\phi}(k_m)\rangle}{\partial z}. \quad \text{(C-6)}$$

It remains to determine how the non-zero impedance of the effective free surface perturbs the mean eigenvalues $\langle k_m\rangle$ of the mean eigenfunctions $\langle\phi\rangle$. Following Kuperman and Ingenito, if the effective depth separated wave equation is multiplied by the conjugate of the eigenfunction and visa-versa; the difference is taken, and we then divide by the local density ρ and integrate over depth, we obtain

$$\int_{-\infty}^{0}dz\frac{\langle\phi\rangle''\langle\phi\rangle^*}{\rho}-\int_{-\infty}^{0}dz\frac{\left(\langle\phi\rangle^*\right)''\langle\phi\rangle}{\rho}=i4\Im\left\{\langle k_m\rangle\right\}\Re\left\{\langle k_m\rangle\right\}\int_{-\infty}^{0}dz\frac{\langle\phi\rangle\langle\phi\rangle^*}{\rho}. \quad \text{(C-7)}$$

Further, if we integrate the first integral on the left hand side of equation (C-7) twice by parts we get an expression in the field and it's derivative evaluated at the free surface and a term which cancels with the second integral, yielding

$$\left.\frac{\langle\phi\rangle'\langle\phi\rangle^*}{\rho}\right|_0=i4\Im\left\{\langle k_m\rangle\right\}\Re\left\{\langle k_m\rangle\right\}\int_{-\infty}^{0}dz\frac{\langle\phi\rangle\langle\phi\rangle^*}{\rho}. \quad \text{(C-8)}$$

Insertion of the effective surface impedance condition (equation C-6) into equation (C-8), division by the common factor *i* and taking the real part, the depth integral on the right hand side of equation (C-8) reduces to the identity and we are left with an expression for the imaginary part of the wavenumber $\Im\{k_m\}$ in terms of the derivative of the mean mode shape function $\langle\phi\rangle$ at the surface, the real part of a spectral integral of the sea surface

power spectrum multiplied by the local vertical wavenumber, the real part of the modal wavenumber and the surface density and sound speed

$$\Im\{\langle k_m \rangle\} = \left|\langle \phi \rangle'\right|^2 \frac{1}{8\pi\rho\Re\{\langle k_m \rangle\}} \Re\left\{\int dq \sqrt{\omega^2/c(0)^2 - q^2}\, P(k_m - q)\right\}. \qquad \text{(C-9)}$$

In evaluating equation (C-9) it is usual to assume that the real part of the mean modal wavenumber $\langle k_m \rangle$ is equal to the unperturbed eigenvalue k_m, and likewise with the derivative of the mode shape function at the surface.

Using the WOA 1 degree historical sound speed database, and previously computed mode shape functions for mode 1, equation (C-9) was evaluated over the surface of the earth for a sea surface spectrum corresponding to the Pierson-Moskowitz model (see Kuperman's papers for a definition of this spectrum) for winds blowing in the direction of acoustic propagation. These calculations were performed for Winter (Jan-Mar) and Summer (Jun-Aug) for several wind speeds at 10 and 50 Hz. The results for a 20 m/s wind speed (corresponding to roughly 40 knots) in Winter are illustrated for 50 Hz in Figure C-1. This is likely to be the worst case for our problem, since losses will increase with frequency, windspeed and interaction with the surface (winter). The attenuations at 50 Hz range from 10^{-3} to 10^{-1} dB/km at the high latitudes, and are negligible in the mid latitudes . Similar calculations at 10 Hz show attenuations from 10^{-5} to 10^{-3} dB/km at the high latitudes, and are again negligible in the mid latitudes. Comparison with Figure C-2 shows the reason: modes only interact with the surface at high latitudes, where the surface is cold and the corresponding sound speed is upward refracting. In equation (C-9) the slope of the mode shape function is only significant in the high latitudes. Put another way, modes in the SOFAR channel in the mid latitudes are insensitive to surface roughness and hence suffer negligible attenuation. It should be noted that the regions of surface interacting modes for the 10 and the 50 Hz cases show some variation; with the 10 Hz region being larger due to the increased width of the mode function. There are also seasonal fluctuations; in the winter the modes interact with more surface waters in the northern latitudes, while during the northern summer there is more extensive surface interaction in the extreme southern latitudes.

Modal attenuations for surface wind speeds of 10 and 5 m/s are much lower, especially at 5 m/s, where the attenuations may be considered negligible at all locations

Since surface interaction and upward refracting sound speed files are often associated with ice cover, and since the modal attenuations associated with ice cover are higher than the attenuations computed here for even the 20 m/s wind speeds associated with gales, we conclude that the modal attenuations due to surface interaction with wind driven waves are a second order effect compared to the effects of ice cover.

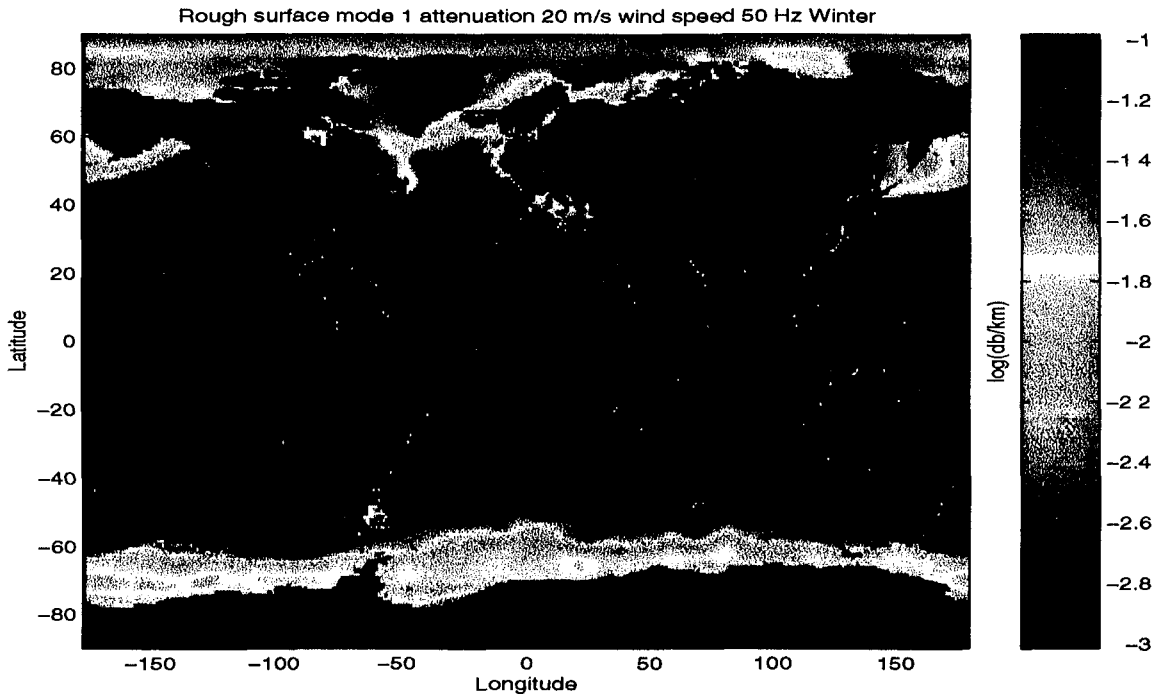

Figure C-1: Mode 1 attenuation in dB/km at 50 Hz for 20 m/s wind speed in the winter (corresponding to the most significant surface interaction in the northern hemisphere.)

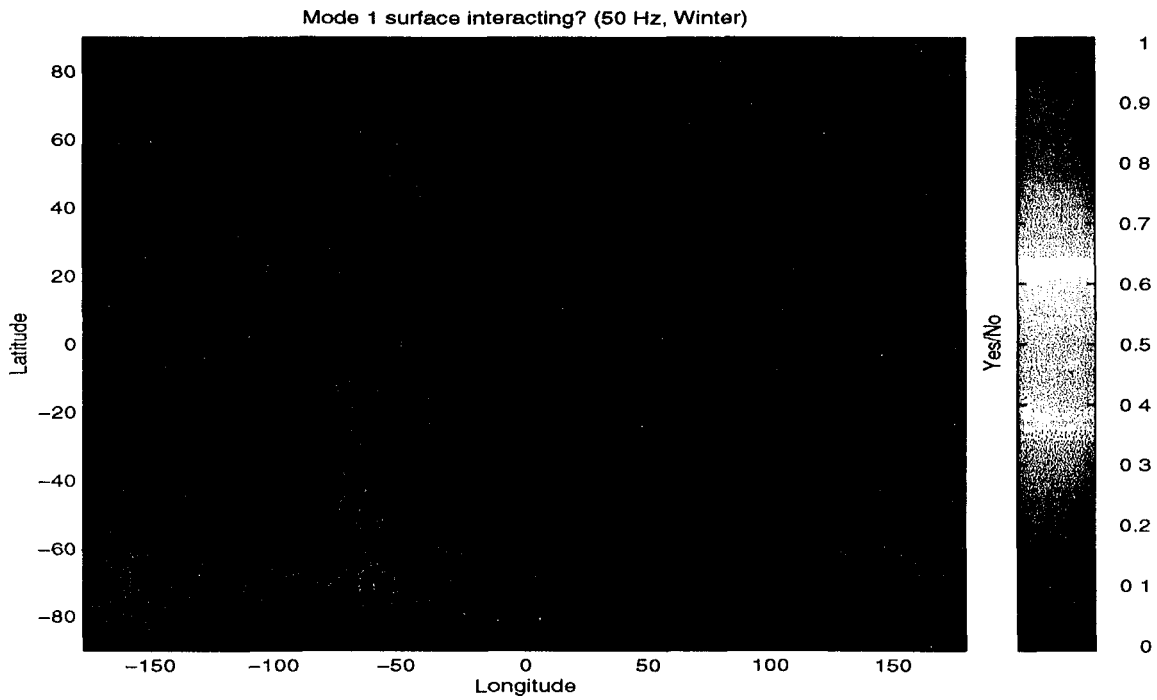

Figure C-2: Regions of mode 1 surface interaction at 50 Hz in winter world wide. Note the significant surface interaction in the northern hemisphere, consistent with cold surface temperatures during winter.

References

[C1] K.D. LePage, *Surface Interaction Attenuation*, BBN Internal Memorandum, June 27, 1997.

[C2] W. A. Kuperman, *Coherent component of specular reflection and transmission at a randomly rough two-fluid interface*, J. Acoust. Soc. Am.**58**, No. 2, 365-370 (1975)

[C3] W. A. Kuperman and F. Ingenito, *Attenuation of the coherent component of sound propagating in shallow water with rough boundaries*, J. Acoust. Soc. Am.**61**, No. 5, 1178-1187 (1977).

Appendix D: Classified Appendix

This appendix is provided in a separate document.